Low Loss Waveguides and AI-designed Optical Couplers for Breath Sensing

韓, 瑜

Low Loss Waveguides and AI-designed Optical Couplers for Breath Sensing

Interdisciplinary Graduate school of Engineering Science,

Kyushu University

Hamamoto Laboratory

Yu Han

Table of contents

Abstract

Population ageing is becoming one of the most significant issues in twenty-first century. One of the consequences of a population aging is its challenge on public health care. Compared to the traditional blood or urine tests, breath content detection is less stress to human body to collect and real time for health-monitoring. As a result, for the early detection of lifestyle diseases, breath sensing is gaining more attention.

For home-use, breath sensor based on infrared absorption spectroscopy has the possibility to sense several kinds of gases at the same time. This is because each gas has its own eigen absorption peak in wavelength. To achieve the effectively long length sensing path (corresponding km order) within a cavity, CRDS (cavity ring-down spectroscopy) has been proposed. One issue of the traditional CRDS system as home-use sensor is its large size.

For bring the possibility of integrating the whole CRDS system into a cell phone for real-time health-monitoring, we propose a future version of CRDS photonic integrated circuit. On the circuit, the optical devices, including the sensing

waveguides, optical power couplers and polarization rotators, are critical for realizing compact and highly sensitive CRDS. In previous work, we have proposed low-loss SiO_2 high-mesa waveguides for the breath sensing. One issue of preventing further ppm-order detection is the low portion of evanescent light (Γ_{air}=2.2%). In order to realize low propagation loss α and high Γ_{air} simultaneously, we have researched 100 nm thick Si high-mesa waveguides in this work. Si has much higher refractive index (3.45) than that of the doped SiO_2 (1.48) at the wavelength of 1.55 μm, which enables a narrower waveguide width and a larger fraction of the mode residing beside the sidewalls. The calculated results confirm that Γ_{air} of Si high-mesa waveguides is much higher than that of the previous SiO_2. After fabrication, α of the Si waveguides is still high and the thermal oxidation technique is applied to further reduce α. After thermal oxidation, α is effectively reduced from 1.45 to 0.84 and 0.29 to 0.2 dB/cm for the 0.5 and 3μm-wide waveguide, respectively. The reduction of α is attributed to the decrease of the sidewall scattering loss and the damaged Si absorption loss. The high Γ_{air} and effective loss reduction show a promising potential of applying Si high-mesa waveguides to realize ppm-order sensing.

Optical power coupler is one of the well-used components in integrated photonics. Although couplers with an output power ratio 1:1 have been widely studied in the past, constructing asymmetric-ration optical power couplers is still an issue, which is difficult to be addressed by using traditional Y-branch waveguides. Artificial intelligence (AI) deep learning is an effective technique for realizing complex optical structures. In this work, two asymmetric couplers with a splitting power ratio of 1:9 and 1:99 have been designed via deep learning method. To realize the asymmetric ratios, the coupler region was divided into discrete nano-pixels in the shape of circular holes with the same dimension. Deep learning was utilized to decide the material of each hole to be waveguide or air one by one and FDTD simulation was introduced to evaluate the performance of the AI designed couplers. The splitting power ratio of 1:9.007 and 1:99.004 has been realized in the two couplers with a same footprint of $3.4 \times 3.2\ \mu m^2$. In addition, the positions and widths of the output waveguides were further optimized as the excess loss of the couplers is a bit high of more than 3.50 dB. Through the optimization of the configuration, a scattering loss reduction of 1.7 dB by position optimization, and a coupling loss reduction of 1.6 dB by width widening were confirmed. The

achieved design exhibited an operation wavelength from 1500-1600 nm and a sufficient fabrication tolerance of ±10 nm (± 11%).

In the development of photonic integrated circuits (PICs), polarization management is an important research topic because of the polarization-dependency of the optical waveguide devices. Polarization rotators, therefore, are often used to manipulate the polarization state of optical wave. Traditional rotators are either with a large size, a complex fabrication or a high excess loss. In this work, a polarization rotator designed with deep learning has been proposed and demonstrated. The total footprint of the rotator is $2.1 \times 12.58\ \mu m^2$ with the polarization extinction ratio of 25.8 dB and the excess loss of 0.17 dB. Furthermore, the proposed rotator exhibits sufficient fabrication tolerance of ±10 nm (±6.7%).

The demonstrated optical devices will pave the way for developing compact CRDS integrated photonic circuits.

Chapter 1 Introduction

1.1 Research background

Population ageing is becoming one of the most significant issues in twenty-first century [1]. According to data from World Population Prospects (the 2017 Revision) [2], 12.5% people worldwide was older than 60. As shown in Fig. 1.1, in 2050, older persons, defined as the age ≥ 65 [2], are projected to account for 20% people globally. Although the process of population ageing is most advanced in Europe and Northern America, where more than 20% persons was older than 60 in 2017, the populations of other regions are growing older as well. In 2050, persons with age ≥ 65 are expected to account for 35% of the population in Europe, 28% in Northern America, 25% in Latin America and the Caribbean, 24% in Asia, 23 % in Oceania and 9% in Africa.

One of the consequences of a population aging is its challenge on public health care [3]. The health-monitoring for older people will become one of the serious issues in the coming future. There have been some regular health-monitoring methods, such as the traditional blood [4], urine [5], cough [6] and other tests,

which help us to identify a disorder or disease. And there are a lot of techniques to identify the presence of microorganism inside the body, like ultrasound [7], magnetic resonance imaging [7], eco-cardiogram [8], and others. So far, these methods are still time consuming and requiring professional support to identify the results.

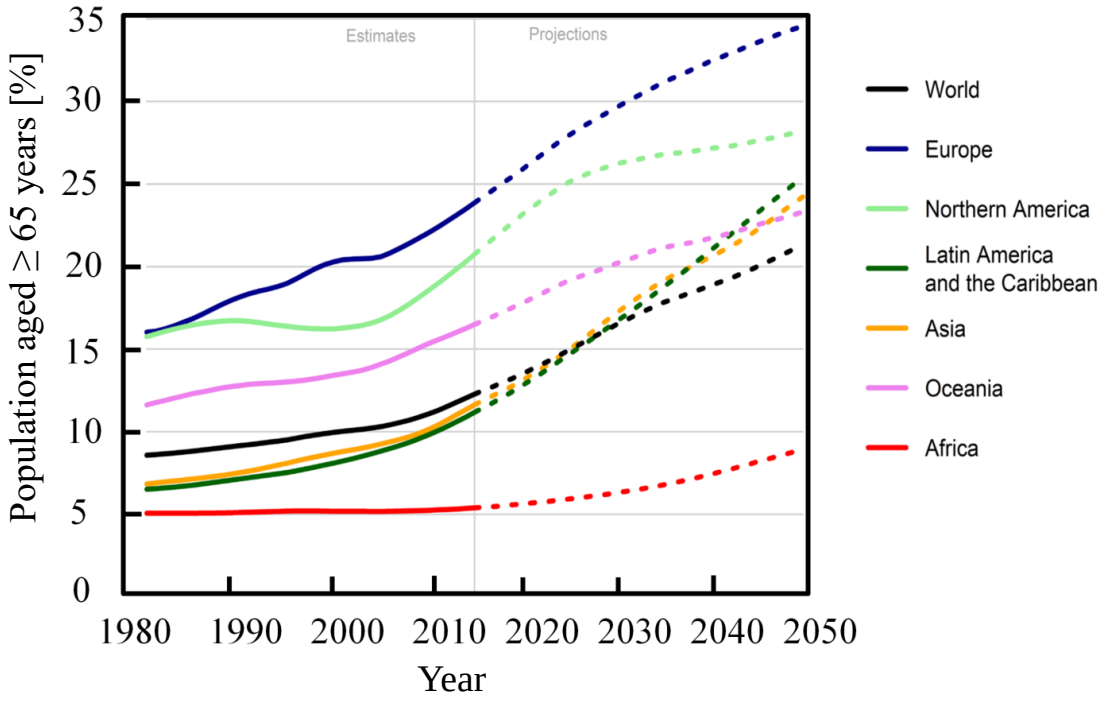

Fig. 1.1 Percentage of population aged ≥ 65 years in the world, from 1980 to 2050 [2]. Population aging problem continues, and even accelerates.

On the other hand, a person's breath includes tiny concentrations of gases that are closely associated with bodily functions and disease, such as high blood pressure, diabetes, and cancer [9]. Compared to the traditional blood or urine tests,

breath content detection is less stress to human body to collect and real time for health-monitoring [10]. As a result, for the early detection of lifestyle diseases, breath sensing is gaining more attention in examining the gas components of a person's breath as biomarkers of the person's body.

Table 1.1 Breath contents with their concentration in exhaled breath and the name of their indicative diseases. The breath contents have potential for sensing many kinds of diseases.

Breath content	**Concentration in breath**	**Name of the disease**	**Ref.**
CH_4 (Methane)	2-10 ppm	Buerger disease	[11]
C_2H_6 (Ethane)	10 ppb	Rheumatic fever, Diabetes mellitus	[12]
CO (Carbon monoxide)	1-10 ppm	Lung disease	[13]
NO (Nitric Oxide)	10-50 ppb	Allergy of trachea system	[14]
NH_3 (Ammonia)	0-1 ppm	Kidney and renal failure	[15]
COS (Carbonyl Sulphide)	0-10 ppb	Lung transfer with acute rejection	[13]
C_5H_8 (Isoprene)	50-200 ppb	Cholesterol biosynthesis	[16]
CH_3COCH_3 (Acetone)	0-1 ppm	Diabetes	[16]

The composition of exhaled breath (excluding saturated water vapor) is about 80% nitrogen (N_2), 16% oxygen (O_2), and 4% carbon dioxide (CO_2). The rest part is less than 1%; however, the rest includes important volatile gases as diseases markers [17-19]. As shown in Tab. 1.1, a number of marker molecules have been identified in breath that could be utilized to identify disease. The concentration of these gases in exhaled breath indicates the potential of some diseases.

1.2 Breath sensing: state of the arts

Sensing exhaled breath is one of the easy ways of health check. Based on the sensing principle, the gas sensors are divided into indirect sensing type and direct sensing type. We summarized the research of the gas sensors in Tab. 1.2 (indirect sensing type) and Tab. 1.3 (direct sensing type).

Indirect sensing relies on the reaction between gas and some materials, through measuring the generated change of resistance, refractive index, frequency, or the transmittance to estimate gas concentration [20]. The indirect type sensors have high sensing sensitivity. Usually, the indirect type sensors are suitable for sensing gas concentration burst change. Indirect type sensors utilizing in daily health care may have drift problem. The

sensing part's surface may get dirty or damage after several times using. The drift problem may result in low sensing accuracy. Moreover, the sensing target gas must be decided. Breath sensor with only one kind of gas sensing contains little health information.

Table 1.2 Indirect sensing type: they have high sensitivity. The sensing target gas must be decided.

Institute	Principle	Size (mm^3)	Detectable gas	Ref.
AIST (Japan)	Resistance change (semiconductor sensor)	5 ×5 ×1	N^2	[21]
Hitachi (Japan)	Resistance change (semiconductor sensor)	30 ×40 ×5	Alcohol	[22]
Royal Institute of Tech. (Sweden)	Resistance change (semiconductor sensor)	10 ×10 ×1	H_2S	[23]

Table 1.3 Direct sensing type: they are possible for sensing many kinds of gases. It is available for daily use.

Institute	Principle	Size (mm^2)	Detectable gas	Ref.
Tohoku Univ. (Japan)	UV spectroscopy	600×600	All kinds	[24]
Toshiba (Japan)	Infrared spectroscopy		All kinds	[25]
Univ. Dusseldorf (Germany)	Infrared spectroscopy	600×800	All kinds	[26]

Direct sensing estimates the change of gas physical quantities, such as mass-sensitive [27], chromatography [28], and infrared absorption spectroscopy [25, 26]. The direct sensing type sensors have gas selectivity in addition to real-time sensing. Among the direct sensing techniques, infrared optical absorption has the advantages of ability of measuring multiple gasses and superior ppm-order sensitivity to various types of breathing contents. Different gases have their inherent absorption wavelength as shown in Tab. 1.4, so, response of the absorption wavelength is unique to the investigated breath content.

Table 1.4 Breath contents with their absorption wavelength and absorption cross section [23-26]. Different gas has its eigen absorption wavelength.

Breath gas	**Absorption wavelength [μm]**	**Absorption cross section [cm^2]**
CO_2	1.572	7.7×10^{-23}
CH_3COCH_3	2.12	4.2×10^{-22}
	1.69	3.6×10^{-22}
NH_3	3.00	1.2×10^{-19}
	1.51	2.5×10^{-20}
CH_4	3.24	1.7×10^{-18}
	1.651	1.6×10^{-20}
NO	5.26	6.1×10^{-19}
	2.67	1.2×10^{-20}

The gas concentration can be deduced through their absorption cross sections through Beer-Lambert law [22]. In Beer-Lambert law, the gas and its concentration are derived as:

$$P_1=P_0\exp(-\alpha L) \quad (1.1)$$

where P_0 is the power of the illumination of the illumination received by the breath gas, P_1 the power of illumination after the absorption by the breath gas, α is the linear absorption coefficient per unite length, and L is the length of the optical path. The absorption coefficient α is defined as follows:

$$\alpha = \sigma n \tag{1.2}$$

where σ is the gas absorption cross section and n the gas concentration. Based on Eq. (1.1) and (1.2), the analysis of measured absorption spectra by applying Beer-Lambert law allows us to determine the presence of specific gases and their concentrations.

As mentioned in Tab. 1.1, the gas concentration in exhaled breath is all at ppm-order. For sensing ppm-order breathing component by using infrared absorption spectroscopy, an extremely long optical sensing path of several km is needed for sufficient light absorption. To achieve the effective long-length sensing path (corresponding km order), cavity ring-down spectroscopy (CRDS) method has been has been exploited [29-31]. CRDS [29-31] obtains ring-down pulse by injecting optical pulse into gas cavity of which both ends are consisted from high reflection mirrors as shown in Fig. 1.2. As reflected back light corresponds to the extension of effective optical path length, this method is useful for highly sensitive detection. During the reflection happens, a small portion of the optical pulse comes out from the high reflection mirror and is detected as output pulses. In such a manner, ring-down pulse intensity follows exponentially decreasing curve shown in right-hand

side of Fig. 1.2. In case a certain portion of detecting gas exits in the cavity, the ring-down time, which is defined as a decay time of 1 / e pulse intensity compared to the initial pulse one, decreases due to gas absorption (Fig. 1.2 (b)) compared to the case of vacuum as shown in Fig. 1.2 (a). The gas concentration is estimated by the ring-down time difference between the ring-down time without gas absorption and with gas absorption. If we use a meter-long cavity in CRDS for instance, the effective length may exceed km order.

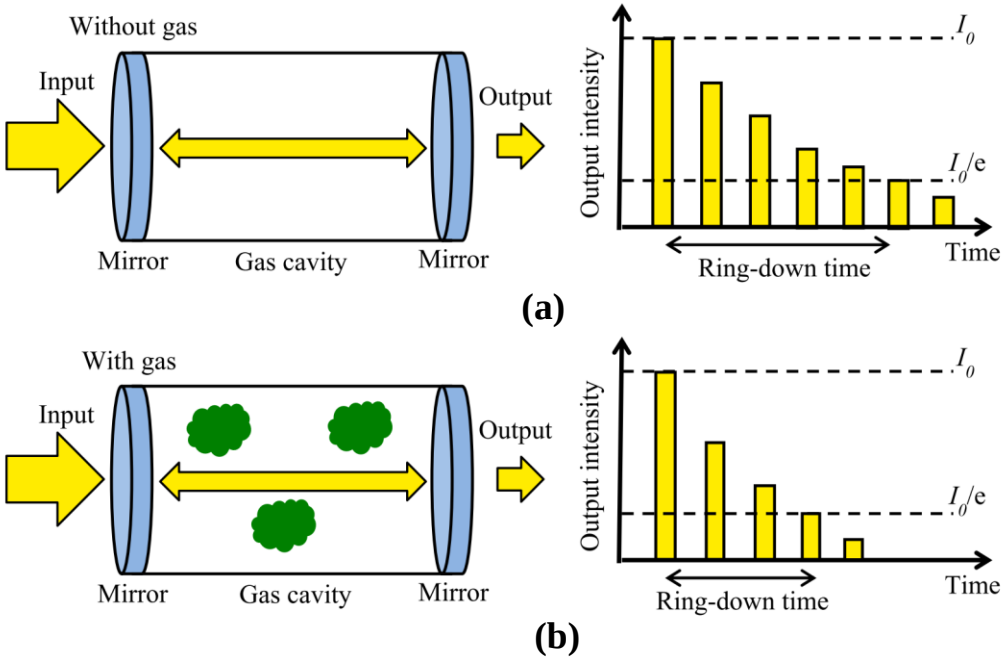

Fig. 1.2 Schematic of ring-down pulse in CRDS system: (a) Without gas and (b) With gas. By using a meter-long cavity in for instance, the effective length may exceed km order.

One issue of the CRDS system as home-use sensor is its

large cavity size, making it an unsuitable choice for daily health check. In order to realize a compact CRDS that is able to be integrated into smart phone for real-time health-monitoring, our research focus on photonic integrated circuits (PICs) [32-36] based on optical waveguides. This is because PICs realizes bulk CRDS (several m^2) integrating in a compact area ($1cm^2$) [37-42].

1.3 Photonic integrated circuits for compact CRDS

To bring the possibility of integrating the whole CRDS system into a cell phone for real-time health-monitoring, we design a future version of photonic integrated circuits (PICs) as shown in Fig. 1.3. The expected size of the chip is only 1 cm^2.

The sensing path and the mirrors in the conventional CRDS system [32-36] have been replaced by an optical waveguide and coupler, which are integrated on one chip, respectively. Signal light from the tunable laser diode (LD) is injected into the sensing waveguide via an optical coupler. The sensing light is absorbed by gas while propagating through the waveguide. When the sensing light propagates to the end port of the waveguide, 1% portion of light is guided to photo detector for detecting light intensity via the 1:99 coupler. The rest part of the

sensing light is guided back to the input port of the waveguide for gas absorption. As most of the signal light loops back into the cavity, the equivalent path length corresponds to a few hundred meters in length which contributes to high sensitivity like ppm-order gas detection. The semiconductor optical amplifier (SOA) is used to compensate the propagation loss of the sensing waveguide [37]. When the SOA is pumped, it may start lasing after its light power reach to the lasing threshold. This lasing phenomenon is called self-lasing. When self-lasing happens, the gain of the signal light will be weak while the gain of self-lasing light is increasing. We, therefore, have to eliminate the self-lasing. In a ring laser, lasing happens when coherency is secured, which means the traveling light wave keeps the same frequency and polarization condition during a roundtrip in the cavity. To suspend the self-lasing, we proposed the scheme of polarization direction control via a polarization rotator. By changing the polarization direction of the traveling light wave during loops back in the cavity, to prevent the traveling light from lasing [39].

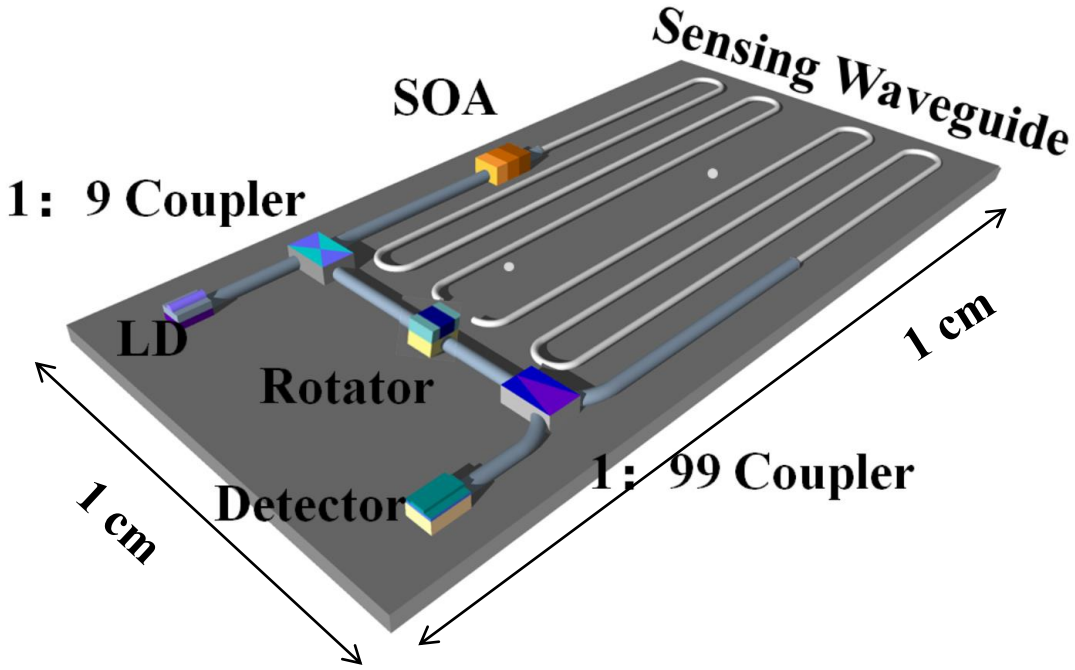

Fig. 1.3 Future vision of CRDS chip for ppm-order breath-sensing: CRDS is integrating on a 1 cm^2 size chip.

In addition, the waveguide length determines the total loss of the chip. Its length should be shorter than the value where SOA can compensate the waveguide loss. In the sensing cavity, the noise is mainly from the SOA. This is caused by the amplified spontaneous emission of SOA. The total noise is accumulated with the increased roundtrip. In our previous work, we have calculated the noise effect. When the input laser is 50mW, the maximum roundtrip is 20000. This roundtrip number satisfies the requirement of acetone gas detection [39].

As shown in Fig. 1.3, the optical components are critical for realizing CRDS photonic circuit. In this thesis, we will focus on the sensing waveguide, couplers and polarization rotator.

1.4 High-mesa waveguides for sensing

To realize optical gas sensing, propagation mode effective index [43], extinction of evanescent field [44], and other sensing techniques with directional couplers [45], Mach-Zehnder interferometers [46], Bragg gratings [47], micro ring resonators [47] and other optical structures have been exploited. The sensing techniques, optical structures and the detected substances are shown in table 1.5. Unlike those complex structures (such as ring resonator or Bragg grating), optical waveguides have been proposed for optical absorption sensing [48-50]. In the waveguide-based breathing sensors, gas-molecules of interest interact with the evanescent electric field outside the waveguide core.

Table 1.5 Reported structures and detected substance. Except high-mesa waveguides, other structures are complex.

Detected substance	**Optical Structure**	**Ref.**
Hydrogen	F-P micro cavity	[51]
Nano particle detection	Nano cavity	[52]
Methyl mercaptan	Optical fiber	[53]
Acetone, ethanol, dichloromethane	Bragg grating	[54]
Isopropanol, water, cyclohexane	Micro ring resonator	[55]
Ethanol	High-mesa waveguide	[56]

To boost light-gas interactions, hollow waveguides [48], slot waveguides [49] and sub-wavelength grating (SWG) waveguides [50] (Fig. 1.4) have been proposed and demonstrated as sensing platforms. In these waveguides, a larger fraction of the mode resides in the low-index cladding where the breathing contents are located. The benefits; however, may be offset by their increased susceptibility to optical loss induced by sidewall-roughness scattering. The large scattering loss limits the total length of the waveguide, resulting in that most

propagated light in the waveguide is lost and little of it interacts with the targeted gas. As a result, efficiently quantifying the trade-off between mode delocalization and scattering loss is critically important for the rational design of chip-scale photonic sensors. In addition, the manufacturing procedure of the hollow, slot and SWG waveguides are usually complex, requiring high-resolution electron-beam lithography.

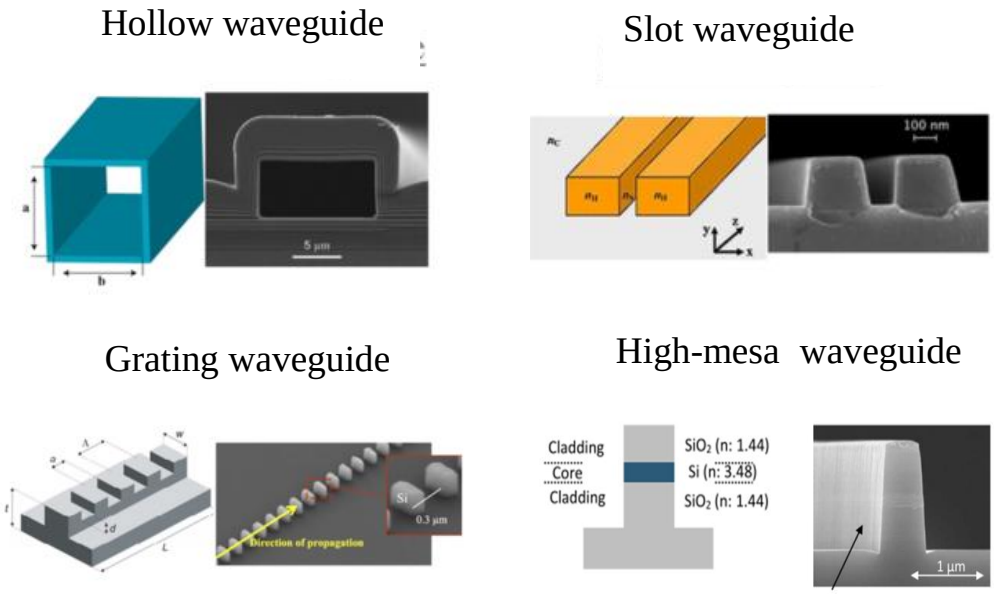

Fig. 1.4 Schematic of hollow [48], slot [49], SWG [50] and high-mesa waveguide structures. Among them, high-mesa waveguides possess the advantages of single-step fabrication and being immune to the dust in air.

To solve above issues, we have proposed high-mesa waveguide structures for the CRDS system [37]. The top

cladding of the high-mesa waveguide protects it from being contaminated by the dust in air. In addition, the high-mesa waveguide is achieved by using single dry-etching process, which promotes the development of integrated photonics and allows it for large-scale production. To compare the above waveguides in details, the characteristics of the waveguides are summarized Table 1.6. As shown in this table, it is clear that high-mesa type waveguide is more suitable for gas sensing than the others.

Table 1.6 Characteristics of the typical waveguides for gas sensing. The high-mesa waveguide is suitable for gas sensing than the others.

Waveguide type	**Easy for touching gas**	**Easy for fabrication**	**Propagation loss**
Hollow	☹	☹	0.02 dB/cm
Slot	☺	☹	12 dB/cm
Grating	☺	☹	6 dB/cm
High-mesa	☺☺	☺☺	0.02-0.2 dB/cm

An extremely low propagation loss α of 0.02 dB/cm has been achieved in the doped-SiO_2 high-mesa waveguide, and 50% concentration CO_2 was successfully detected [38]. One issue of preventing further ppm-order detection is the low portion of evanescent light (Γ_{air}=2.2%). In order to realize low propagation loss α and high Γ_{air} simultaneously, we have researched 100 nm thick Si high-mesa waveguides in this work. Si has much higher refractive index (3.45) than that of the doped SiO_2 (1.48) at the wavelength of 1.55 μm, which enables a narrower waveguide width and a larger fraction of the mode residing beside the sidewalls. The calculated results confirmed that Γ_{air} of Si high-mesa waveguides is much higher than that of the previous SiO_2.

1.5 Optical power couplers

As shown in Fig. 1.3, optical power couplers are a key component in the gas sensing chip due to the requirements of power distribution. An optical power coupler is a waveguide optical power distribution device, which plays an important role in passive optical network [57-61]. One typical optical power coupler is the Y-branch waveguide that has an input waveguide and two output waveguides as shown in Fig. 1.5 (a). Symmetric

Y-branch 3-dB couplers (output power ratio 1:1) are wavelength-independent and have been studied to some extent in the past [57]. In contrast, couplers with an asymmetric splitting ratio still have difficulties that are not easily addressed for practical applications. For realizing asymmetric splitting ratios, asymmetric Y-branch waveguides, directional couplers and multi-mode interferometer (MMI) waveguides have to be implemented [58-61]. In the asymmetric Y-branch waveguides, the cross-section of the input waveguide is different from those of the output waveguides, so that it is difficult to realize optical mode-matching among the waveguides. This may cause a high coupling loss from the input waveguide to the output waveguides. Another structure for realizing couplers is the directional couplers as shown in Fig. 1.5(b). The issues for the directional couplers are that the coupling section is long and the operation wavelength bandwidth is limited [62-65]. For example, for a silicon channel waveguide directional coupler, the length of the coupling section is around 20 μm and the bandwidth is only 5 nm when the change of the splitting ratio is less than 5% [62]. For MMI waveguides, there is not any principle for directing the design of asymmetric optical power couplers [61].

On the other hand, if asymmetric optical power couplers can

be easily designed, it is valuable for integrated optics. For example, a little amount of the light is able to be coupled out from some part of a densely integrated photonic circuit by using asymmetric couplers, so that the power or wavelength is liberally monitored with less power-loss [66].

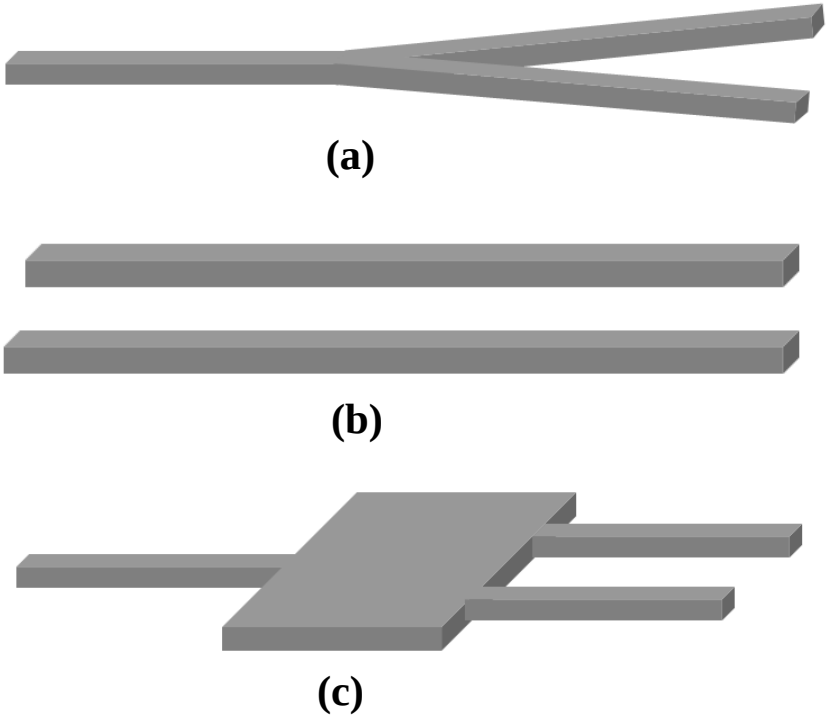

Fig. 1.5 Top-view schematics of (a) Y-branch optical power coupler [34], (b) Directional coupler [36] and (c) MMI optical power coupler [61].

In this thesis, we have designed asymmetric-ration optical power couplers by using deep learning design. Two couplers with the targeted splitting power ratio as 1:9 and 1:99 have been designed, respectively. Table 1.7 shows the comparison of Y-branch, directional coupler and AI deep learning design

optical power couplers. As shown in this table, it is clear that deep learning design waveguide is more suitable for asymmetric optical power couplers than the others. In this thesis, we have designed asymmetric-ration optical power couplers by using AI deep learning design.

Table 1.7 Comparison of the waveguides for optical power couplers. AI deep learning design waveguide is more suitable for asymmetric optical power couplers than the others.

Waveguide type	**Symmetric optical power couplers**	**Asymmetric optical power couplers**	**Device length**
Y-branch	☺	☹	10 μm
Directional coupler	☺	☹	100 μm
MMI	☺	☹	50 μm
AI design	☺	☺	< 20μm

1.6 Polarization Rotators

In the development of PICs, polarization management is an important research topic because of the strong polarization-dependent performance of the optical waveguides

[67]. Polarization rotators are often used to manipulate the polarization state of optical wave. Normally, they are separate components, and their individual footprints are relatively large, seriously limiting the integration applications [68].

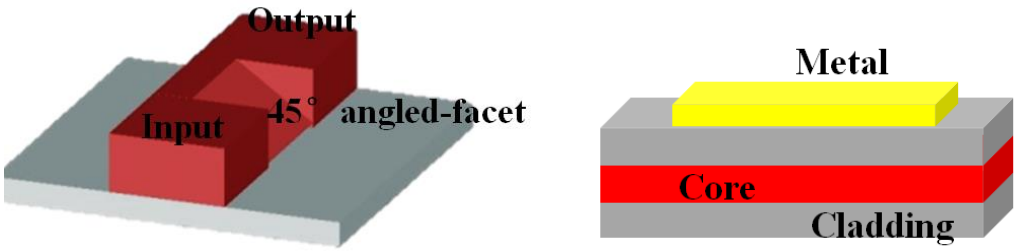

(a) **(b)**

Fig. 1.6 Previous two typical polarization rotators (a) 45° angled-facet waveguide and (b) Surface plasma waveguide. Both of them have drawbacks hindering their applications.

To shrink the size of rotator, various approaches have been proposed, such as 45° angled-facet waveguides, surface plasma waveguides and so on [69-74]. For the angled-facet waveguide rotators as shown in Fig. 1.6(a), it requires two different etching steps (wet and dry etching) to form the asymmetric structure of waveguide, i.e., an angled and a vertical sidewall [69-74]. It is a difficult process; however, to realize an accurately 45° angled sidewall. For the surface plasma waveguide rotators as shown in Fig. 1.6 (b), it consists of a metal on the top of the cladding [75-77]. Though the rotator is compact, the metal-on-cladding

may induce extra absorption loss. A new scheme with both a simple structure and good performance, therefore, is urgently needed.

In this thesis, we have designed a polarization rotator by using deep learning design. The total space of the rotator is 2.1 × 12.58 μm^2 with a polarization extinction ratio of 28.8 dB and an excess loss of 0.17 dB. The achieved design also exhibited an operation wavelength ranging from 1570-1680 nm in addition to a fabrication tolerance of ±10 nm (± 6.7%). Table 1.8 shows the comparison of the above mentioned polarization rotators. As shown in this table, it is clear that AI deep learning design waveguide is more suitable for polarization rotators than the others.

Table 1.8 Comparison of the waveguides for polarization rotators. AI assisted design waveguide is more suitable for polarization rotators than the others.

Waveguide type	**Easy for fabrication**	**Excess loss**	**Device length**
45 °angled-facet	☹	☺	1000 μm
Surface plasma	☺	☹	100 μm
AI design	☺	☺	< 20μm

1.7 Thesis construction

In this thesis, the research background and the purpose have been explained in Chapter 1. Breath content detection for easy medical health motoring has been proposed using CRDS system. In order to overcome the drawbacks of the traditional bulk CRDS equipment, a future vision of the CRDS PICs has been proposed for measuring ppm-order components in human breath within a compact area. High-mesa waveguides, optical power couplers and polarization rotators are the key components in the CRDS PICs.

In Chapter 2, the high-mesa waveguide parameters, i.e. propagation loss and portion of evanescent light, for ppm-order gas sensing have been discussed. Deep learning photonic device design have been introduced and several examples about the complex optical nanostructures via deep learning design have been also demonstrated.

In Chapter 3, 100 nm thick Si high-mesa waveguides have been researched. The designed optical constructions are able to provide a high portion of evanescent light, which is critical for ppm-order breath content sensing. Thermal oxidation technique has been exploited to reduce optical loss. The obtained propagation loss is as low as 0.85 and 0.20 dB/cm for the 0.5 and 3 μm wide Si high-mesa waveguides. As a result, a photonic circuit based on the Si high-mesa waveguides is expected to sense ppm-order breath content for health-monitoring.

In Chapter 4, 1:9 and 1:99 optical power couplers based on deep learning have been described. Both couplers occupy a compact area of $3.4 \times 3.2\ \mu m^2$ with a low excess loss and a wide wavelength operation range. Furthermore, the proposed couplers have a large fabrication tolerance, which will benefit for the fabrication.

In Chapter 5, we have designed a polarization rotator by using deep learning design. The total space of the rotator is 2.1 × 12.58 μm^2 with a polarization extinction ratio of 28.8 dB and an excess loss of 0.17 dB. The achieved design also exhibited an operation wavelength ranging from 1570-1680 nm in addition to a sufficient fabrication tolerance of ±10 nm (± 6.7%).

In Chapter 6, the above results have been summarized and clarified about the future view of the proposed PICs for infrared absorption sensing.

1.8 References

[1] United Nations, http://www.un.org/en/sections/issues-depth/ageing/

[2] Population Division, Department of Economic and Social Affairs, United Nations Secretariat, http://population.un.org/wpp/

[3] P. Zhang, X. Zhang, J. Brown, D. Vistisen, R. Sicree, J. Shaw and G. Nichols, "Global healthcare expenditure on diabetes for 2010 and 2030," Diabetes Res. Clin. Prac. 87, 293-301 (2010).

[4] Wikipedia, http://en.wikipedia.org/wiki/Blood_test

[5] Wikipedia, http://en.wikipedia.org/wiki/Urinalysis

[6] H. D. Bennett, L. J. M. T. Tambeur, and W. B. Campbell, "Use of coughing test to diagnose peritonitis," BMJ. 308, 1336 (2004).

[7] S. Ogawa, T. M. Lee, A. R. Kay, and D W Tank "Brain magnetic resonance imaging with contrast dependent on blood oxygenation," PNAS 87 (24), 9868-9872 (1990)

[8] P. S. Douglas, M. J. Garcia, D. E. Haines, W. W. Lai, W. J. Manning, A. R. Patel, M. H. Picard and D. M. Polk, "Appropriate Use Criteria for Echocardiography," J. Am. Coll. Cardiol. 57,1126-1166 (2011).

[9] G. Konvalina and H. Haick, "Sensors for Breath Testing: From Nanomaterials to Comprehensive Disease Detection," Acc. Chem. Res. 47, 66-76 (2014).

[10] A. Lanzarotta, L. Lorenz, S. Voelker, T. M. Falconer and J. S. Batson, "Forensic Drug Identification, Confirmation, and Quantification

Using Fully Integrated Gas Chromatography with Fourier Transform Infrared and Mass Spectrometric Detection (GC-FT-IR-MS),” Appl. Spectrosc. 72, 750-756 (2018).

[11] Tiger Optics, http://www.tigeroptics.com/app/tigeroptics/products/

[12] M. Murtz, “Breath Diagnostics Using Laser Spectroscopy,” OPN 16, 30-35 (2005).

[13] W. Cao and Y. Duan, “Current status of methods and techniques for breath analysis,” Crit. Rev. Anal. Chem. 37, 3–13 (2007).

[14] Ekips Technology, http://www.ekipstech.com/

[15] Picarro, http://www.picarro.com/gasesmeasured/

[16] T. H. Risby and S. F. Solga, “Current status of clinical breath analysis,” Appl. Phy. B 85, 421-426 (2006).

[17] A. Amann, P. Spanel and D. Smith, “Breath analysis: the approach towards clinical applications,” Mini-Rev. Med. Chem. 7, 115–129 (2007).

[18] G. Giubileo, “Medical diagnostics by laser-based analysis of exhaled breath,” Proc. SPIE 4762, 318–325 (2002).

[19] L. Amorimb and Z. Cardeal, “Breath air analysis and its use as a biomarker in biological monitoring of occupational and environmental exposure to chemical agents,” J. Chromatogr. B 853, 1–9 (2007).

[20] S. Yang, C. Jiang, and S. Wei, “Gas sensing in 2D materials,” Appl.

Phys. Rev. 4, 021304 (2017).

[21] T. Itoh, D. Nagai, and W. Shin, “Development of sensor device for breath analysis”, Sansouken Today, 12-13 (2013).[in Japanese]

[22] H. Wakana, M. Yamada, and M. Sakairi, “Portable alcohol detection system with breath- recognition function,” 2018 IEEE Sensors. IEEE, 1-4 (2018).

[23] H. Gatty, G. Stemme, and N. Roxhed, “A miniaturized amperometric hydrogen sulfide sensor applicable for bad breath monitoring,” Micromachines 9 (12), 612 (2018).

[24] T. Iwata, T. Katagiri, and Y. Matsuura, “ Real-time analysis of isoprene in breath by using ultraviolet-absorption spectroscopy with a hollow optical fiber gas cell,” Sensors 16 (12), 2058 (2016).

[25] R. Ueno, K. Ishii, K. Suzuki, and H. Funaki, “Infrared multispectral imaging with silicon-based multiband pass filter and infrared focal plane array,” 2015 9th International Conference on Sensing Technology (ICST). IEEE, 211-214 (2015).

[26] M. Murtz, D. Halmer, M. Horstjann, S. Thelen, P. Hering, “Ultrasensitive trace gas detection for biomedical applications,” Spectrochim. Acta A, 63, 963-969 (2005).

[27] K. Ballschmiter, M. Zell, “Analysis of polychlorinated biphenyls (PCB) by glass capillary gas chromatography,” Fresenius' Z Anal. Chem. 302, 20–31 (1980).

[28] D. Naviglio, L. Grottaglie, M. Vitulano, M. Trifuoggi, and M. Gallo, “Characterization of Essential Oil Components from Aromatic Plants that Grow Wild in the “Piana del Sele” (Salerno, Southern Italy) using Gas Chromatography-Mass Spectrometry,” Nat. Prod. Commun. 10 (7), 1293 (2015).

[29] M. Mazurenka, A. Orr-Ewing, R. Peverall, and G. Ritchieb, “Cavity ring-down and cavity enhanced spectroscopy using diode lasers,” Annu. Rep. Prog. Chem. C 101, 100–42 (2005).

[30] J. B. Dudek, P. Tarsa, A. Velasquez, M. Wladyslawski, P. Rabinowitz, and K. Lehmann, “Trace moisture detection using continuous-wave cavity ring-down spectroscopy,” Anal. Chem. 75, 4599–605 (2003).

[31] H. Abe and K. Yamada, “Performance evaluation of a trace-moisture analyzer based on cavity ring-down spectroscopy: direct comparison with the NMIJ trace- moisture standard,” Sens. Actuators A 165, 230 (2011).

[32] M. Haurylau, G. Chen, H. Chen, J. Zhang, N. A. Nelson, D. H. Albonesi, E. G. Friedman, and P. M. Fauchet, “On-chip optical interconnect roadmap: challenges and critical directions,” IEEE J. Sel. Top. Quantum Electron. 12 (6), 1699–1705 (2006).

[33] C. Gunn, “CMOS photonics for high-speed interconnects,” IEEE. Micro. 26 (2), 58–66 (2006).

[34] A. Shacham, K. Bergman, and L. P. Carloni, “Photonic

networks-on-chip for future generations of chip multiprocessors," IEEE Trans. Comput. 57 (9), 1246–1260 (2008).

[35] D. Miller, "Device requirements for optical interconnects to silicon chips," Proc. IEEE 97 (7), 1166–1185 (2009).

[36] K. Preston, L. Chen, S. Manipatruni, and M. Lipson, "Silicon photonic interconnect with micrometer-scale devices," 6th International Conference on Group IV Photonics, WA2, 1–3 (2009).

[37] J. Chen, H. Hokazono, D. Nakashima, M. Tsujino, Y. Hashizume, M. Itoh, and K. Hamamoto, "Low loss silica high-mesa waveguide for infrared sensing," Jpn. J. Appl. Phys. 53, 022502 (2014).

[38] H. Hokazono, W. Li, S. Enami, H. Jiang, and K. Hamamoto, "Gas sensing demonstration by using silica high-mesa waveguide with amplified cavity ring down spectroscopy technique," IEICE Electron. Expr. 15, 1-8 (2015).

[39] W. Li, Y. Han, Z. Chen, H. Jiang, and K. Hamamoto, "Amplifier-assisted CRDS (cavity ring-down spectroscopy) toward compact breath sensing," Jpn. J. Appl. Phys. 58, SJJD01 (2019).

[40] D. Nakashima and K. Hamamoto, "Proposal of Novel Strip High-Mesa Waveguide for Infrared Absorption Sensing," Appl. Phys. Express 5, 062202 (2012).

[41] A. Intekhab, "SOI-based Si/SiO_2 High-mesa Waveguide for Optical Absorption Sensing," Thesis, Kyushu Univ. (2013).

[42] J. Chen, H. Hokazono, D. Nakashima, M. Tsujino, Y. Hashizume, M. Itoh, and K. Hamamoto, “Proposal of multi-slot silica high-mesa waveguide for infrared absorption,” IEICE Electron. Expr. 10, 1-7 (2013).

[43] A. Densmore, D. X. Xu, P. Waldron, S. Janz, P. Cheben, J. Lapointe, A. Delâge, B. Lamontagne, J. H. Schmid, and E. Post, “A Silicon-on-insulator photonic wire based evanescent field sensor,” IEEE Photon. Technol. Lett. 18, 2520-2522 (2006).

[44] K. E. Zinoviev, A. B. Gonzalez-Guerrero, C. Dominguez and L. M. Lechuga, “Integrated Bimodal Waveguide Interferometric Biosensor for Label-Free Analysis,” J. Light. Technol. 29. 1926-1930 (2011).

[45] B. J. Luff, R. D. Harris, J. S. Wilkinson, R. Wilson, and D. J. Schiffrin, “Integrated-optical directional coupler biosensor,” Optics Lett. 21, 618-620 (1996).

[46] F. Prieto, B. Sepulveda, A. Calle, A. Llobera, C. Domynguez, A. Abad, A. Montoya, and L. M. Lechuga, “An integrated optical interferometric nanodevice based on silicon technology for biosensor applications,” Nanotechnology. 14, 907-912 (2003).

[47] W. C. L. Hopman, P. Pottier, D. Yudistira, J. van Lith, P. V. Lambeck, R. M. De La Rue, and A. Driessen, “Quasi-One-Dimensional Photonic Crystal as Compact Building-Block for Refractometric Optical Sensors,” IEEE J. Sel. Topics of Quantum Electron. 11,

11-16, (2005).

[48] C. Shi, “Inner wall coated hollow core waveguide sensor based on double substrate surface enhanced Raman scattering,” Appl. Phys. Lett. 93, 153101 (2008).

[49] F. D. Olio and V. M. Passaro, “Optical sensing by optimized silicon slot waveguides,” Opt. Express15, 4977-4993 (2007).

[50] J. G. Wangüemert-Pérez, “Evanescent field waveguide sensing with subwavelength grating structures in silicon-on-insulator,” Opt. Lett. 39, 4442-4445 (2014).

[51] M. Kozuka, T. Minamide, H. Saito, H. Kudo, K. Otsuka, M. Takao, and K. Mitsubayashi, “An Optical Halitosis (Bad Breath) Sensor with MAO-A,” IEEE Sensors 2006, EXCO, Daegu, Korea (2006).

[52] B. Schmidt, V. Almeida, C. Manolatou, S. Preble, and M. Lipson, “Nanocavity in a silicon waveguide for ultrasensitive nano-particle detection,” Appl. Physc. Lett. 85, 4855 (2004).

[53] M. A. Vincenti, M. De Sario, V. Petruzzelli, A. D’Orazio, F. Prudenzano, D. de Cegliab, and M. Scalora, “Fabry-Perot microcavity sensor for H_2 breath test analysis,” J. of Appl. Phys. 102, 074501 (2007).

[54] F. J. Arregui, I. R. Matías and R. O. Claus, “Optical Fiber Gas Sensors Based on Hydrophobic Alumina Thin Films Formed by the Electrostatic Self-Assembly Monolayer Process,” J. of IEEE Sensors

3, 1 (2003).

[55] C. A. Barrios, K. B. Gylfason, B. Sánchez, A. Griol, H. Sohlström, M. Holgado, and R. Casquel, "Slot-waveguide biochemical sensor," Opt. Lett. 32, 3080-3082 (2007).

[56] S. Yano, K. Kameyama, and K. Hamamoto, "Low loss SOI-based high-mesa waveguides fabricated using neutral loop discharge (NLD) plasma etching for compact breath-sensing system", Con. Proc. Integrated Photonics and Nanophotonics Research and Applications, IWA7, Salt Lake, USA (2007).

[57] J. D. Love and N. Riesen, "Single-, few-, and multimode Y-junctions," J. Lightwave Technol. 30(3), 304–309 (2012).

[58] A. G. Medoks, "Theory of symmetric waveguide Y-junction," Radio Eng. Electron. 13, 106 (1968).

[59] M. Izutsu, Y. Nakai, and T. Sueta, "Operation mechanism of the single-mode optical-waveguide-Y junction," Opt. Lett. 7, 136–138 (1982).

[60] W. Y. Hung, H. P. Chan, and P. S. Chung, "Novel design of wide-angle single-mode symmetric Y-junctions," Electron. Lett. 24, 1184–1185 (1988).

[61] W. M. Henry and J. D. Love, "Asymmetric multimode Y-junction splitters," Opt. Quantum Electron. 29, 379–392 (1997).

[62] E. A. J. Marcatili, "Dielectric rectangular waveguide and directional

coupler for integrated optics," Bell Syst. Tech. J. 48(7), 2071–2102 (1969).

[63] T. Suhara, Y. Handa, H. Nishihara, and J. Koyama, "Analysis of optical channel waveguides and directional couplers with graded index profile," J. Opt. Soc. Am. 69, 807–815 (1979).

[64] R. C. Alferness, C. H. Joyner, L. L. Buhl, S. K. Korotky, "High-speed traveling-wave directional coupler switch/modulator for λ = 1.32 μm," IEEE J. Quantum Electron. 19, 1339–1341 (1983).

[65] Q. Li, Y. Song, G. Zhou, Y. Su, and M. Qiu, "Asymmetric plasmonic-dielectric coupler with short coupling length, high extinction ratio, and low insertion loss," Opt. Lett. 35, 3153–3155 (2010).

[66] Y. Han, W. Li, Z. Hui Chen, H. Jiang, and K. Hamamoto, "Fabrication and analysis of low loss silicon high-mesa waveguides," Appl. Opt. 59 (16), 4964-4969 (2020).

[67] W. Bogaerts, R. Baets, P. Dumon, V. Wiaux, S. Beckx, D. Taillaert, B. Luyssaert, J. V. Campenhout, P. Bienstman, and D. V. Thourhout, "Nanophotonic waveguides in silicon-on-insulator fabricated with CMOS technology," J. Lightwave Technol. 23, 401 – 412 (2005).

[68] T. Barwicz, M. R. Watts, M. A. Popović, P. T. Rakich, L. Socci, F. X. Kärtner, E. P. Ippen, and H. I. Smith, "Polarization-transparent microphotonic devices in the strong confinement limit," Nat.

Photonics 1, 57 (2007).

[69] H. Fukuda, K. Yamada, T. Tsuchizawa, T. Watanabe, H. Shinojima, and S. Itabashi, “Silicon photonic circuit with polarization diversity,” Opt. Express 16(7), 4872–4880 (2008).

[70] N. Somasiri, B. M. A. Rahman, and S. S. A. Obayya, “Fabrication tolerance study of a compact passive polarization Rotator,” J. Lightwave Technol. 20 (4), 751–757 (2002).

[71] H. Deng, D. O. Yevick, C. Brooks, and P. E. Jessop, “Design rules for slanted-angle polarization rotators,” J. Lightwave Technol. 23 (1), 432–445 (2005).

[72] C. Brooks, P. E. Jessop, H. Deng, D. O. Yevick, and G. Tarr, “Passive silicon-on-insulator polarization-rotating waveguides,” Opt. Eng. 45 (4), 044603 (2006).

[73] H. Deng, D. O. Yevick, C. Brooks, and P. E. Jessop, “Fabrication tolerance of asymmetric silicon-on-insulator polarization rotators,” J. Opt. Soc. Am. A. 23 (7), 1741–1745 (2006).

[74] L. M. Augustin, J. J. G. M. van der Tol, E. J. Geluk, and M. K. Smit, “Short Polarization Converter Optimized for Active–Passive Integration in InGaAsP–InP,” IEEE Photon. Technol. Lett. 19 (20), 1673–1675 (2007).

[75] Komatsu, K. Saitoh, and M. Koshiba, “Compact polarization rotator based on surface plasmon polariton with low insertion loss” IEEE

Photonics J. 4, 707–714 (2012).

[76] L. Gao, Y. Huo, J. S. Harris, and Z. Zhou, “Ultra-compact and low-loss polarization rotator based on asymmetric hybrid plasmonic waveguide,” IEEE Photonics Technol. Lett. 25 (21), 2081–2084 (2013).

[77] J. N. Caspers, J. S. Aitchison, and M. Mojahedi, “ Experimental dem-onstration of an integrated hybrid plasmonic polarization rotator,” Opt. Lett., 38 , 4054 – 4057 (2013).

Chapter 2 Breath sensing principle and artificial intelligence deep learning design

2.1 Breath sensing principle

2.1.1 Infrared absorption spectroscopy

In general, each target gas has its own eigen absorption wavelength at infrared band as shown in Table 1.4. The amount of the absorbed infrared light intensity is determined by the density of the gas molecule N [molecule/cm^3], the gas absorption cross-section σ [cm^2 /molecule], and the interaction length L [cm] between the sensing light and the target gas. The relationship of the light intensity, N, σ, and L is expressed as [1]:

$$\frac{I_{out}}{I_{in}} = \exp(\sigma NL) \tag{2.1}$$

Here, I_{in} and I_{out} are the input and output light intensity, respectively. The density of the gas molecule N [molecule/cm^3] is expressed as [2],

$$N = \frac{NA \times n}{V_{total}} \tag{2.2}$$

NA [number/mol] is Avogadro constant [3]. In breath sensing, n [mol] is the amount of the target gas. V_{total} [cm^3] is the total volume of the breath. Gas concentration N' [ppm] is expressed by V_{total} and the volume of the target gas V_{gas} [cm^3] as:

$$N' = \frac{V_{total}}{V_{gas}} \times 10^{-9} \quad (2.3)$$

Based on the Ideal gas law [4] which is

$$PV_{gas} = nRT \quad (2.4)$$

The density of the gas molecule N could be express by gas concentration N' as:

$$N = \frac{P \times NA}{RT} \times N' \times 10^{-9} \quad (2.5)$$

Here, P [Pa] is pressure, T [K] is temperature, R [m^3 ·Pa/mol·K] is ideal gas constant. Based on Eq. (2.1) and (2.5), the relationship between the sensing light and gas concentration N' is expressed as:

$$\frac{I_{out}}{I_{in}} = \exp(-\sigma L \times N' \times \frac{P \times NA}{RT} \times 10^{-9}) \quad (2.6)$$

To measure ppm-order gases in exhaled breath by using infrared absorption spectroscopy, the sufficient gas absorption (typically 3 dB) is desired [5]. We set the criteria of "3 dB difference" between I_{out} and I_{in} to estimate the necessary interaction length L for some ppm-order breath contents. The estimated results are summarized in Tab. 2.1, with the breath content names, their absorption cross-section σ, absorption wavelength λ [μm], the related disease [6-11], and the required interaction length L [km] for sensing their concentration N [ppm] in exhaled breath.

Table 2.1 Ppm-order breathing components and their needed sensing path length. The required sensing path lengths are all at km-order.

Gas	λ [μm]	N' [ppm]	σ [cm^2/molecule]	Disease	L [km]
Methane	1.65	2-10	1.6×10^{-20}	Intestine	20
Ammonia	1.51	0.5-5	2.5×10^{-20}	Liver	25
Acetone	1.68	1.7-3.7	3.6×10^{-22}	Diabetes	2309

As shown in Tab. 2.1, km-order length of sensing path is needed for the ppm-order gas concentration detection in exhaled breath by using infrared absorption spectroscopy. This extremely long sensing path is impossibly realized in hand-held size sensor.

2.1.2 Waveguide CRDS for ppm-order gas sensing

As mentioned in Chapter 1.2, CRDS system realizes the corresponding km-order sensing path in a gas-cell. The problem of general CRDS as hand-held sensor is its large gas-cell size. To realize hand-held sensor, we proposed a future vision of CRDS photonic chip as shown Fig. 2.1, in which the high-mesa waveguide is used as the optical sensing path instead of the gas-cell.

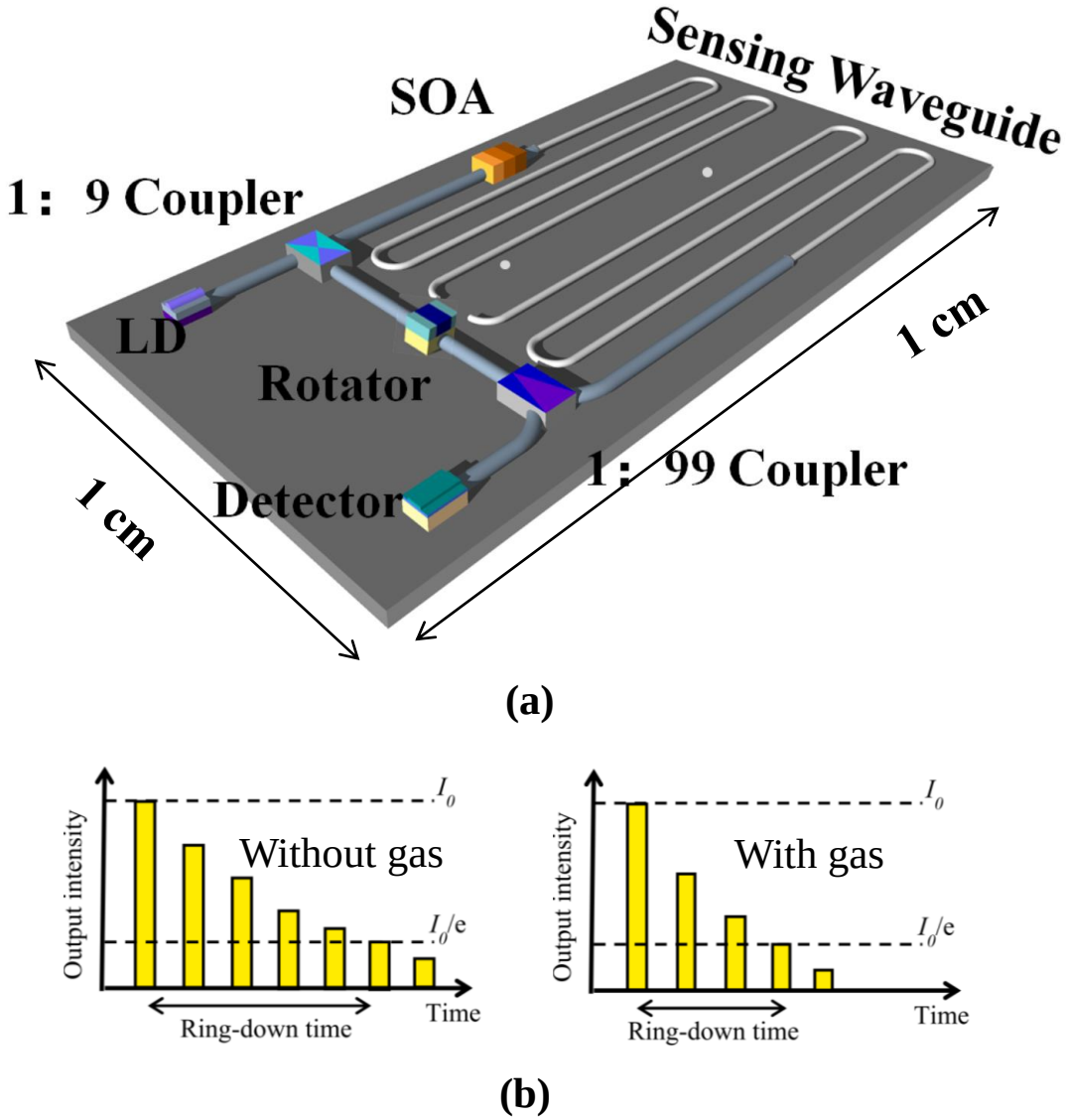

Fig. 2.1 Waveguide CRDS sensing (a) Future vision of CRDS chip for ppm-order breath-sensing and (b) target gas concentration estimated by using ring-down time difference with / without gas.

When the sensing light propagates in the high-mesa waveguide, a portion of the light goes out of the waveguide. This portion of light intensity is used for gas absorption. Gas absorption happens by using waveguide as the sensing path. We

precisely solved the mode distribution. Figure 2.2 shows the light intensity of the propagation mode profile. Air region works as cladding in this waveguide. The refractive index difference between the waveguide and air is huge. So, boundary condition is no more secured. That's why the intensity is once enhanced just at the outside of the waveguide, and then decay. So, relatively high portion of the light exits at the outside.

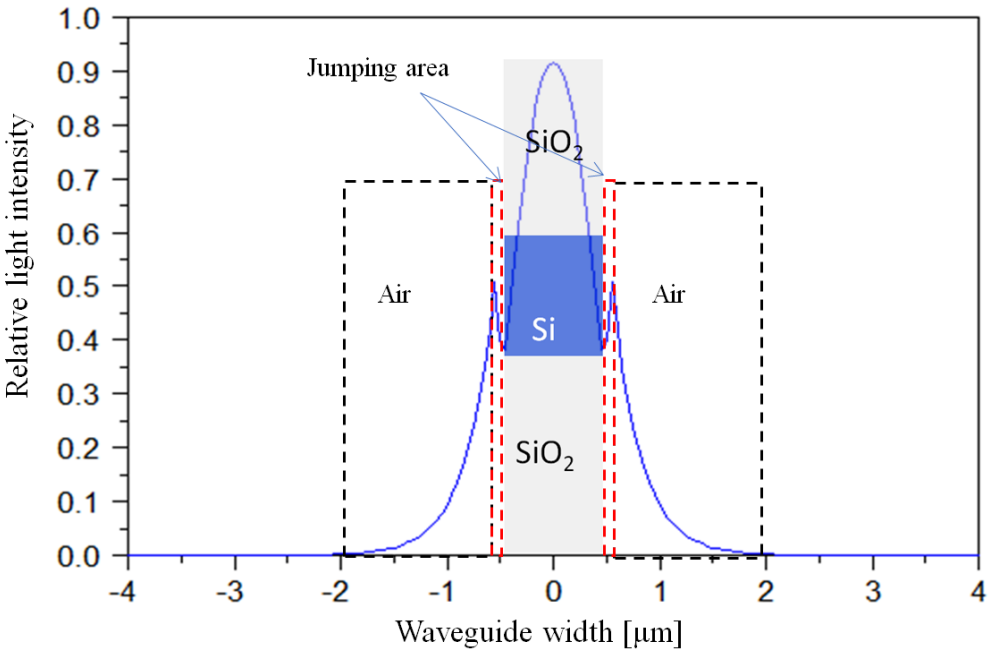

Fig. 2.2 Light intensity of propagation mode profile

In the waveguide CRDS, gas concentration is estimated by the cavity ring-down time [12-20]. As shown in Fig. 2.1, cavity ring-down time is related to the number of the pulses. The ring-down time is the time at which the light intensity falls to 1/e of the initial intensity (I_0). The pulse number during the ring

down time difference is called the ring-down number. To distinguish the cavity ring-down time difference between "without gas" and "with gas" situation, the ring-down number between is,

$$m\text{-}m(gas)=1 \tag{2.7}$$

Here, *m* and *m(gas)* is the pulse number during the ring down time without and with gas, respectively.

At the situation of "without-gas", the light intensity of the last pulse in pulse train I_{out} is [21]:

$$I_{out} = I_0 \times \left[G \times Loss_{system}\right]^m \tag{2.8}$$

And at the situation of "with gas", the light intensity of the last pulse in pulse train $I_{out(gas)}$ is:

$$I_{out(gas)} = I_0 \times \left[G \times Loss_{system} \times Loss_{abs.}\right]^{m(gas)} \tag{2.9}$$

G is the semiconductor optical amplifier (SOA) gain, and $Loss_{system}$ indicates the system loss, including the waveguide propagation loss and the couplers/ rotator losses. $Loss_{abs.}$ is the gas absorption loss. When the pulse intensity reaches to the criteria level (normally 1/e), we have:

$$I_{out} = I_{out(gas)} = 1/e\ I_0 \tag{2.10}$$

By combining Eq. (2.7) and (2.10), we summarized Eq. (2.8) and (2.9) as:

$$I_0 \times \left[G \times Loss_{system}\right]^{m(gas)+1} = I_0 \times \left[G \times Loss_{system} \times Loss_{abs.}\right]^{m(gas)}$$

(2.11)

The required number of pulses *m(gas)* is calculated as:

$$m(gas) = Log_{Loss_{abs.}}(G \times Loss_{system}) \quad (2.12)$$

Based on Eq. 2.6, $Loss_{abs}$ is expressed as:

$$Loss_{abs.} = \exp(-\sigma L \times N' \times \frac{P \times NA}{RT} \times \Gamma_{air} \times 10^{-9}) \quad (2.13)$$

As mentioned in Chapter 1.3, Γ_{air} is the portion of the light goes out of the waveguide (known as evanescent field). The waveguide length L could be expressed by the waveguide total loss $Loss_{waveguide}$ and waveguide propagation loss α as:

$$L = \frac{Loss_{waveguide}}{\alpha} \quad (2.14)$$

The waveguide performance evaluation constant *FOM* is defined as:

$$FOM = \frac{\Gamma_{air}}{\alpha} \quad (2.15)$$

By using Eq. (2.14) and (2.15), the part of "L× Γ_{air} " in Eq. (2.13) is expressed by *FOM* as:

$$L \times \Gamma_{air} = Loss_{waveguide} \times FOM \quad (2.16)$$

The gas absorption loss $Loss_{abs.}$ could be estimated by setting the total waveguide loss $Loss_{waveguide}$ and the waveguide performance constant *FOM* as:

$$Loss_{abs.} = \exp(-\sigma \times N' \times \frac{P \times NA \times 10^{-9}}{RT} \times L_{waveguide} \times FOM) \quad (2.17)$$

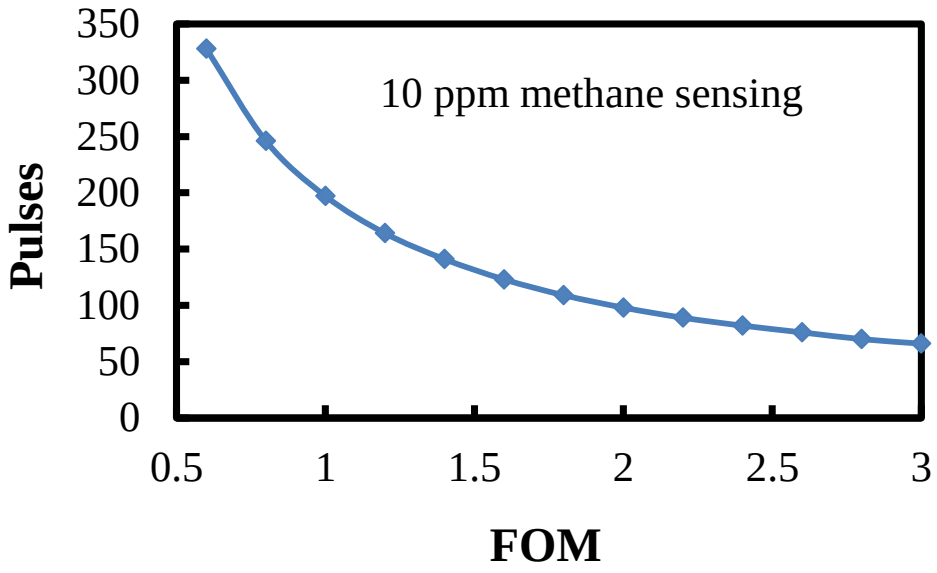

Fig. 2.3 The relationship between the high-mesa waveguide FOM and necessary pulse number for 10 ppm methane sensing : this result shows that 10 ppm methane is possible by using the waveguide CRDS

As shown in Table 2.1, 2-10 ppm methane in the breath content indicates the intestine disease. Thus, for instance, we estimate the high-mesa waveguide FOM and necessary pulse number for 10 ppm methane by using the waveguide CRDS. The total CRDS chip loss is set as 32.5 dB, including 30 dB waveguide loss and 2.5 dB loss from the couplers and rotator. The gain of the SOA is set as 32.4 dB. Based on Eq. (2.12) and (2.17), the relationship between the FOM and necessary pulse number is shown in Fig. 2.3. The result shows that 10 ppm order methane is possible by using the waveguide CRDS.

2.2 AI deep learning design

2.2.1 Challenges of traditional optical design

Photonic integrated circuits have tremendously changed the data telecommunication, calculation and sensing landscape in the last ten to fifteen years [22-30]. Photonics technologies are still expected to progress far beyond, making everyday lives smoother and safer and dramatically improving the efficiency of businesses. To meet the growing demand on high-speed communication (e.g. 5G, big-data) and biological sensing, photonic integrated circuits (PIC) are becoming more and more complicated and the requirement on the device performance and compactness is also increasing exponentially [31-35].

Traditional photonic design method starts with representing the device structure with a set of parameters, such as width, length, radius, etc. Then the parameters are scanned in some range, and optical simulations are carried out for each device structure represented by some combination of the parameters. The results of the devices are calculated from the optical simulations. The traditional design method has led to many useful devices in the past, its limitation becomes apparent when designing more a complicated device [36]. The difficulty originates from the fact that each optical simulation is very time

consuming, so we can only afford to scan a very small set of parameters. As a result, the actual design space is very limited. For example, we need to arrange 20×20 holes in a photonic crystal waveguide as shown in Fig. 2.2 and each hole could be filled with the waveguide material or air. If we use the traditional design method to try each hole one by one (filled with the waveguide or air), the full simulation requires $2^{400}=10^{120}$ times to obtain the optimized structure. Usually, one time of FDTD (finite-difference time-domain method) simulation takes at least 1 min [37], 10^{120} times simulation is unrealistic.

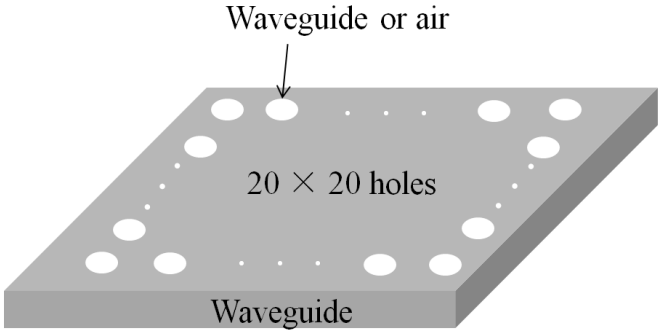

Fig. 2.2 Schematic of a photonic crystal waveguide with 20×20 holes: each hole could be filled with the waveguide material or air. It will take 10^{120} simulations to obtain the optimized structure, which is unrealistic.

2.2.2 Optical design via AI deep learning

The recent blossoming of artificial intelligence (AI), especially

deep learning, has revolutionized photonic design [38-40]. The technique of AI design is considered as a promising candidate for the design of complicated photonic devices. In general, the role of AI in photonic design is also to search the parameters for a best fit of the target. Unlike the traditional method, AI is able to navigate in a smarter way by learning from a large dataset so that a solution can be found in a fast way. This scheme shortens the overall computation time. In this section, we will introduce deep learning.

Inspired by the biological neural networks, deep learning (DL) models the relationship between their inputs and outputs by cascading various nonlinear computational units (known as neurons) [41-43] (Fig. 2.3). DL learns the desired relationship between inputs and outputs by tuning each neuron in response to a training set. Training optimization algorithms are used to strategically introduce these datasets into the neural network and gradually update the network's parameters until a convergence criterion is met. DL parameters like the number of layers, the number of neurons and so on, all affect the final performance.

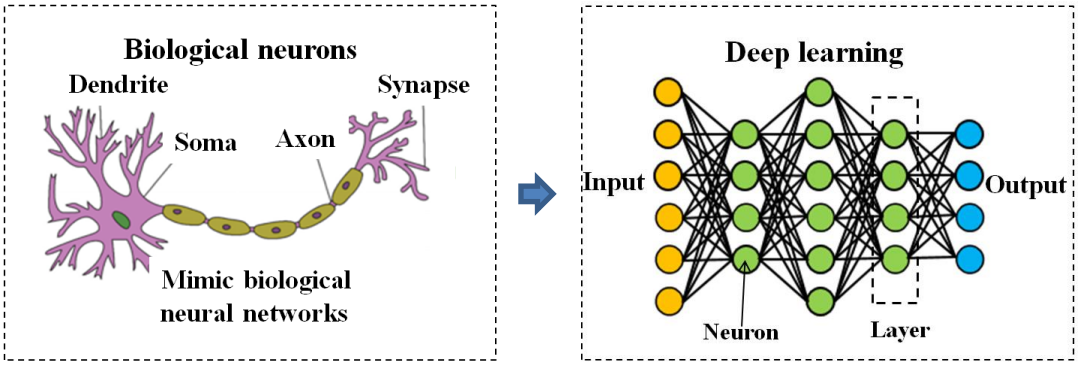

Fig. 2.3 Inspired by the biological neural networks, the deep learning (DL) has been applied in AI optical design. DL models the relationship between their inputs and outputs by cascading various nonlinear computational units, known as neurons and layers.

Several recent reports in the literature have focused on the application of DL to solve complex problems in integrated photonics. Hammond and co-workers demonstrated desiging chirped Bragg grating by using DL [44]; Gostimirovic and co-workers reported the use of DL in the accelerated design of polarization insensitive sub-wavelength grating couplers on a SOI (silicon-on-insulator) platform [45]. The DL optimizes sub-wavelength grating based couplers which is independent of input light polarization [45]. Bor and co-workers introduced DL to design photonic integrated devices showing improved performance compared to traditional design techniques [46]. Asano and co-workers reported DL to optimize the Q factors of

two-dimensional photonic crystal [47]. So far, there have been some other successful applications of DL in the design of complex photonic devices [48-51], which verifies that DL is a powerful tool in optical design.

Table 2.2 State-of-art photonic devices based on AI optical design. AI optical design offers a path for rapid design of complex structures for targeted functions which are difficult to be realized by using traditional design.

Device	**Design Method**	**Institute**	**Ref.**
Grating coupler	Deep learning	Carleton Univ.	[45]
Light transmitter	Deep learning	Osaka Univ.	[46]
Photonic crystal	Deep learning	Kyoto Univ.	[47]
Coupler & rotator	Deep learning	This work	

Table 2.2 shows the state-of-art photonic devices based on AI deep learning optical design. These techniques allow us to go beyond physical insights and help to search the parameter space in a more efficient way. In this work, we will apply AI deep learning to design optical power couplers and polarization rotator.

2.5 Conclusions

In this chapter we first introduced the principle of infrared absorption spectroscopy. Based on these two gas sensing principles, we discussed the possibility of using waveguide sensing CRDS photonic chip to detect breath content. The results show that the ppm-order breath sensing is possible by using the waveguide CRDS photonic chip.

In order to design the optical power couplers and polarization rotator, we compared the traditional optical design method and AI deep learning design method. The traditional design method has led to many useful devices in the past, its limitation becomes apparent when designing more a complicated device. In contrast, AI deep learning design has the ability to solve the problem. In this work, we will choose deep learning method to explore the nano photonic patterns for the desired devices.

2.6 References

[1] D. F. Swinehart, “The beer-lambert law,” J. of Chem. Educ. 39(7), 333-335 (1962).

[2] M. Kawasaki, and S. Enami, “Detection of trace species with cavity ring-down spectroscopy,” Laser Rev. 34(4), 289-294 (2006).

[3] P. D. Bievre, and H. S. Peiser, “Atomic weight’: The name, its history, definition, and units,” Pure and Appl. Chem. 64(10), 1535-1543 (1992).

[4] A. Laugier, and J. Garai, “Derivation of the ideal gas law,” J. of Chem. Educ., 84(11), 1832-1833 (2007).

[5] Z. Q. Liu, and R. L. Wang, “Gas detection with infrared absorption principle,” Coal Sci. and Tech. 1, 21-23 (2005).

[6] D. Roccarina, E. C. Lauritano, M. Gabrielli, F. Franceschi, V. Ojetti, and A. Gasbarrini, “The role of methane in intestinal disease,” The Am. J. of gastroenterol. 105(6), 1250-1256 (2010).

[7] H. Zan, W. Tsai, Y. Lo, Y. Wu, and Y. Yang, “Pentacene-based organic thin film transistors for ammonia sensing”, IEEE Sens. J. 12(3), 594-601 (2011).

[8] K. Kao, M. Hsu, Y. Chang, S. Gwo, and J. Andrew Yeh, “A sub-ppm acetone gas sensor for diabetes detection using 10nm thick ultrathin

InN FETs,” Sens. 12(6), 7157-7168 (2012).

[9] C. Turner, C. Walton, S. Hoashi, and M. Evans, “Breath acetone concentration decreases with blood glucose concentration in type 1 diabetes mellitus patients during hypoglycaemic clamps,“ J. of Breath Res. 3(4), 046004 (2009).

[10] P. Paredi, W. Biernacki, G. Invernizzi, S. A. Kharitnov, and P. J. Barnes, Exhaled carbon monoxide levels elevated in diabetes and correlated with glucose concentration in blood: a new test for monitoring the disease?,” Chest. 116(4), 1007-1011 (1999).

[11] K. Iitani, K. Toma, T. Arakawa, and K. Mitsubayashi, “Transcutaneous blood VOC imaging system (Skin-Gas Cam) with real-time bio-fluorometric device on rounded skin surface,” ACS Sens. 5(2), 338-345 (2019).

[12] J. Chen, H. Hokazono, D. Nakashima, M. Tsujino, Y. Hashizume, M. Itoh, and K. Hamamoto, “Low loss silica high-mesa waveguide for infrared sensing,” Jpn. J. Appl. Phys. 53, 022502 (2014).

[13] H. Hokazono, W. Li, S. Enami, H. Jiang, and K. Hamamoto, “Gas sensing demonstration by using silica high-mesa waveguide with amplified cavity ring down spectroscopy technique,” IEICE Electron. Expr. 15, 1-8 (2015).

[14] W. Li, Y. Han, Z. Chen, H. Jiang, and K. Hamamoto, “Amplifier-assisted CRDS (cavity ring-down spectroscopy) toward compact breath sensing,” Jpn. J. Appl. Phys. 58, SJJD01 (2019).

[15] D. Nakashima and K. Hamamoto, “Proposal of Novel Strip High-Mesa Waveguide for Infrared Absorption Sensing,” Appl. Phys. Express 5, 062202 (2012).

[16] A. Intekhab, “SOI-based Si/SiO_2 High-mesa Waveguide for Optical Absorption Sensing,” Thesis, Kyushu Univ. (2013).

[17] J. Chen, H. Hokazono, D. Nakashima, M. Tsujino, Y. Hashizume, M. Itoh, and K. Hamamoto, “Proposal of multi-slot silica high-mesa waveguide for infrared absorption,” IEICE Electron. Expr. 10, 1-7 (2013).

[18] M. Mazurenka, A. Orr-Ewing, R. Peverall, and G. Ritchieb, “Cavity ring-down and cavity enhanced spectroscopy using diode lasers,” Annu. Rep. Prog. Chem. C 101, 100–42 (2005).

[19] J. B. Dudek, P. Tarsa, A. Velasquez, M. Wladyslawski, P. Rabinowitz, and K. Lehmann, “Trace moisture detection using continuous-wave cavity ring-down spectroscopy,” Anal. Chem. 75, 4599–605 (2003).

[20] H. Abe and K. Yamada, “Performance evaluation of a trace-moisture analyzer based on cavity ring-down spectroscopy: direct comparison

with the NMIJ trace- moisture standard," Sens. Actuators A 165, 230 (2011).

[21] R. W. Ricci, M. Ditzler and L. P. Nestor, "Discovering the Beer-Lambert Law," J. Chem. Educ. 71, 983 (1994).

[22] F. Marsili, V. B. Verma, J. A. Stern, S. Harrington, A. E. Lita, T. Gerrits, I. Vayshenker, B. Baek, M. D. Shaw, R. P. Mirin, and S. W. Nam, "Detecting single infrared photons with 93% system efficiency," Nature Photonics 7, 210 (2013).

[23] L. Chrostowski, Z. Lu, J. Flückiger, J. Pond, J. Klein, X. Wang, S. Li, W. Tai, E. Y. Hsu, C. Kim, J. Ferguson, and C. Cone, "Schematic driven silicon photonics design," Proc. SPIE 9751, 975103 (2016).

[24] S. K. Selvaraja, W. Bogaerts, P. Dumon, D. V. Thourhout, and R. Baets, "Subnanometer linewidth uniformity in silicon nanophotonic waveguide devices using CMOS fabrication technology," IEEE J. Sel. Top. Quantum Electron. 16, 316–324 (2010).

[25] W. A. Zortman, D. C. Trotter, and M. R. Watts, "Silicon photonics manufacturing," Opt. Express 18, 23598–23607 (2010).

[26] N. Ayotte, A. D. Simard, and S. LaRochelle, "Long integrated Bragg gratings for SOI wafer metrology," IEEE Photonics Technol. Lett. 27, 755–758 (2015).

[27] X. Wang, W. Shi, H. Yun, S. Grist, N. A. F. Jaeger, and L. Chrostowski, “Narrow-band waveguide Bragg gratings on SOI wafers with CMOS-compatible fabrication process,” Opt. Express 20, 15547–15558 (2012).

[28] T.-W. Weng, Z. Zhang, Z. Su, Y. Marzouk, A. Melloni, and L. Daniel, “Uncertainty quantification of silicon photonic devices with correlated and non-gaussian random parameters,” Opt. Express 23, 4242–4254 (2015).

[29] D. Melati, A. Melloni, and F. Morichetti, “Real photonic waveguides: guiding light through imperfections,” Adv. Opt. Photonics 6, 156–224 (2014).

[30] Y. Yang, Y. Ma, H. Guan, Y. Liu, S. Danziger, S. Ocheltree, K. Bergman, T. Baehr-Jones, and M. Hochberg, “Phase coherence length in silicon photonic platform,” Opt. Express 23, 16890–16902 (2015).

[31] G. Roelkens, L. Liu, D. Liang, R. Jones, A. W. Fang, B. Koch, and J. E. Bowers, “III–V/silicon photonics for on-chip and intra-chip optical interconnects,” Laser Photonics Rev. 4, 751–779 (2010).

[32] R. Soref, “The past, present, and future of silicon photonics,” IEEE J. Sel. Top. Quantum Electron. 12(6), 1678–1687 (2006).

[33] Y. Arakawa, T. Nakamura, Y. Urino, and T. Fujita, “Silicon photonics for next generation system integration platform,” IEEE Commun. Mag. 51(3), 72–77 (2013).

[34] A. E.-J. Lim, J. Song, Q. Fang, C. Li, X. Tu, N. Duan, K. K. Chen, R. P.-C. Tern, and T.-Y. Liow, “Review of silicon photonics foundry efforts,” IEEE J. Sel. Top. Quantum Electron. 20(4), 405–416 (2014).

[35] X. Luo, J. Song, S. Feng, A. Poon, T. Y. Liow, M. Yu, G. Q. Lo, and D. L. Kwong, “Silicon high-order coupled-microring-based electro-optical switches for on-chip optical interconnects,” IEEE Photonics Technol. Lett. 24(10), 821–823 (2012).

[36] W. Bogaerts, M. Fiers, and P. Dumon, “Design challenges in silicon photonics,” IEEE J. Sel. Top. Quantum Electron. 20, 1–8 (2014).

[37] S. C. Hagness, D. Rafizadesh, S. T. Ho, and A. Taflove, “FDTD microcavity simulations: design and experimental realization of waveguide-coupled single-mode ring and whispering-gallery-mode disk resonators,” J. Lightwave Technol. 15(11), 2154–2165 (1997).

[38] L. Lu, D. Liu, F. Zhou, D. Li, M. Cheng, L. Deng, S. Fu, J. Xia, and M. Zhang, “Inverse-designed single-step-etched colorless 3 dB couplers based on RIE-lag-insensitive PhC-like subwavelength structures,” Opt. Lett. 41(21), 5051–5054 (2016).

[39] M. Teng, K. Kojima, T. Koike-Akino, B. Wang, C. Lin, and K. Parsons, “Broadband SOI mode order converter based on topology optimization,” in Optical Fiber Communication Conference, OSA Technical Digest (Optical Society of America), paper Th2A.8 (2018).

[40] N. Yu and F. Capasso, “Flat optics with designer metasurfaces,” Nature Materials 13, 139–150 (2014).

[41] F. Lussier, D. Missirlis, J. P. Spatz, and J.-F. Masson, “Machine learning driven surface-enhanced raman scattering optophysiology reveals multiplexed metabolite gradients near cells,” ACS Nano 13, 1403–1411 (2019).

[42] H. W. Lin, M. Tegmark, and D. Rolnick, “Why does deep and cheap learning work so well?” J. Stat. Phys. 168, 1223–1247 (2017).

[43] W. Ma, F. Cheng, and Y. Liu, “Deep-Learning-Enabled On-Demand Design of Chiral Metamaterials,” ACS Nano 12, 6326–6334 (2018).

[44] A. M. Hammond, E. Potokar, and R. M. Camacho, “Accelerating silicon photonic parameter extraction using artificial neural networks,” OSA Continuum 2(6), 1964–1973 (2019).

[45] D. Gostimirovic and W. N. Ye, “An Open-Source Artificial Neural Network Model for Polarization-Insensitive Silicon-on-Insulator Subwavelength Grating Couplers,” IEEE J. Sel. Top. Quantum Electron. 25(3), 8200205 (2019).

[46] E. Bor, O. Alparslan, M. Turduev, Y. S. Hanay, H. Kurt, S. I. Arakawa, and M. Murata, “Integrated silicon photonic device design by attractor selection mechanism based on artificial neural networks: optical coupler and asymmetric light transmitter,” Opt. Express 26(22), 29032–29044 (2018).

[47] T. Asano and S. Noda, “Optimization of photonic crystal nanocavities based on deep learning,” Opt. Express 26(25), 32704–32717 (2018).

[48] R. R. Andrawis, M. A. Swillam, M. A. El-Gamal, and E. A. Soliman, “Artificial neural network modeling of plasmonic transmission lines,” Appl. Opt. 55(10), 2780–2790 (2016).

[49] J. Peurifoy, Y. Shen, L. Jing, Y. Yang, F. Cano-Renteria, B. G. DeLacy, J. D. Joannopoulos, M. Tegmark, and M. Soljačić, “Nanophotonic particle simulation and inverse design using artificial neural networks”, Sci. Adv. 4(6), eaar4206 (2018).

[50] Y. Rivenson, Z. Göröcs, H. Günaydin, Y. Zhang, H. Wang, and A. Ozcan, “Deep learning microscopy,” Optica 4(11), 1437–1443 (2017).

[51] Y. Rivenson, Y. Zhang, H. Günaydın, D. Teng, and A. Ozcan, “Phase recovery and holographic image reconstruction using deep learning in neural networks,” Light Sci. Appl. 7(2), 17141 (2018).

Chapter 3 Fabrication and analysis of low loss silicon high-mesa waveguides

3.1 Introductory overview

In previous work, we have proposed high-mesa waveguide structures for the breath sensing CRDS system [1-17]. The top cladding of the high-mesa waveguide protects it from being contaminated by the dust in air, which keeps the accuracy of the measurement as shown in Fig. 3.1. In addition, the high-mesa waveguide is achieved by using single dry-etching process, which promotes the development of integrated photonics and allows it for large-scale production. An extremely low propagation loss α of 0.02 dB/cm has been achieved in the doped-SiO_2 high-mesa waveguide, and 50% concentration CO_2 has been successfully detected [18]. One issue of preventing further ppm-order detection is the low portion of evanescent light (Γ_{air}=2.2%). According to the calculation [18], in order to realize ppm-order detection, the propagation loss $\leq$ 0.05 dB/cm and $\Gamma_{air} \geq$10% are needed.

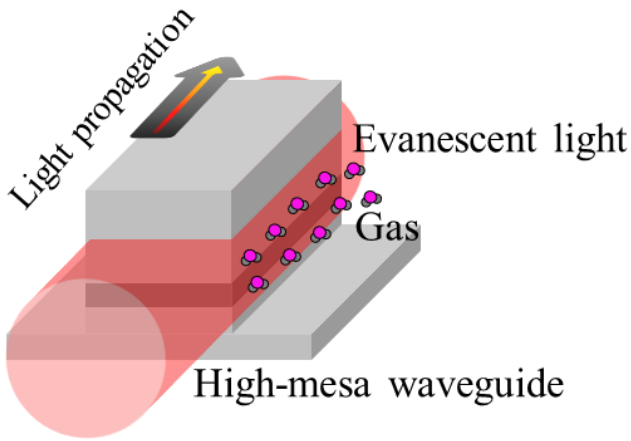

Fig. 3.1 High-mesa waveguide for breath sensing photonic circuit

In order to realize low propagation loss α and high Γ_{air} simultaneously, we have researched 100 nm thick Si high-mesa waveguides in this work. Si has much higher refractive index (3.45) than that of the doped SiO_2 (1.48) at the wavelength of 1.55 μm, which enables a narrower waveguide width and a larger fraction of the mode residing beside the sidewalls. The calculated results confirm that Γ_{air} of Si high-mesa waveguides is much higher than that of the previous SiO_2. After fabrication, α of the Si waveguides is still high and the thermal oxidation technique is applied to further reduce α. After thermal oxidation, α is effectively reduced from 1.45 to 0.84 and 0.29 to 0.2 dB/cm for the 0.5 and 3μm-wide waveguide, respectively. The

reduction of α is attributed to the decrease of the sidewall scattering loss and the damaged Si absorption loss.

3.2 Advantages of 100 nm thin silicon high-mesa waveguides

Figure 3.2 (a) shows the cross-section and fundamental TE modal pattern of the previous SiO_2 high-mesa waveguide at 1550 nm simulated by using beam propagation method [17]. It consists of a GeO_2-doped SiO_2 core with SiO_2 claddings. The thickness of the cover cladding layer, the core, and the under cladding layer is 3, 3.5, and 3.8 μm, respectively. By utilizing this SiO_2 high-mesa waveguide, we have set up a CRDS system where the gas concentration was estimated by the ring-down time difference between the ring-down time without gas absorption and with gas absorption [18]. Then, we demonstrated CO_2 gas with a concentration measurement of 50% for the first time [18]. One of our goals is to detect methane (CH_4) gas from the breath content, because several tens of ppm CH_4 indicates buerger disease in a person [20]. The result of 50% CO_2 gas sensing corresponds to the capability of 500 ppm CH_4 gas sensing because the absorption cross section of CH_4 is 1000 times higher than that of CO_2. According to the calculated results by Lambert-Beer law [17], in order to detect several tens

of ppm CH_4, both low propagation loss < 0.05 dB/cm and Γ_{air} ≥10% should be satisfied simultaneously. Due to the relatively low refractive index of the GeO_2-doped SiO_2 core (1.48), the cut-off condition of the waveguide width is 2 μm, otherwise the mode in the waveguide becomes leaky mode causing high radiation loss. Even with a width of 2 μm, the waveguide still has a quite low Γ_{air} of 2.2%, which obstructs its application in breath sensing.

In contrast, the designed Si high-mesa waveguide in this work (Fig. 3.2 (b)) has much higher refractive index (3.45), which enables a narrower waveguide and a larger fraction of the mode residing beside the sidewalls. The Si high-mesa waveguide is based on a silicon-on-insulator wafer with a device layer of 100 nm, a top SiO_2 cladding of 2 μm and a bottom SiO_2 cladding of 3 μm. The top cladding not only isolates the waveguide core from the upside contamination, but also protects the core in the waveguide fabrication process from the plasma-etching-induced damage. According to the simulated modal pattern, the top cladding should be thicker than 1.2 μm, so a 2 μm top SiO_2 cladding is chosen in this work. As shown in Fig. 3.1 (b), a part of the evanescent field locates near the sidewall of the bottom cladding, so the bottom SiO_2 should be etched in order to

achieve higher Γ_{air}. According to our calculations, a thickness of 1 μm is enough to utilize this evanescent field.

By comparing Fig. 3.2 (a) and (b), the mode horizontally extending out of the waveguide core is much larger for the Si high-mesa waveguide. Figure 3.2 (c) shows the calculated Γ_{air} of the 100 nm Si high-mesa waveguide at different widths. For comparison, the result of previous SiO_2 high-mesa waveguides is also plotted [17]. Obviously, Γ_{air} of the Si waveguide is much higher than that of the SiO_2, and satisfies our requirement of Γ_{air} ≥10%. In future, the high-mesa waveguides will be applied into a CRDS photonic circuit [19], on which there is also integrated tunable laser, optical amplifier and so on. Considering semiconductor-based laser and amplifier are currently the most viable option, Si waveguides should be the most promising option for future integration. In addition, the higher refractive index of Si waveguide is helpful for reducing the footprint of the CRDS photonic chip. According to our simulation by finite-difference time-domain method, the bending loss of the Si high-mesa waveguide is lower than 0.05 dB when the bending radius is larger than 18 μm. All above predict the strong application possibility of the Si high-mesa waveguides in CRDS.

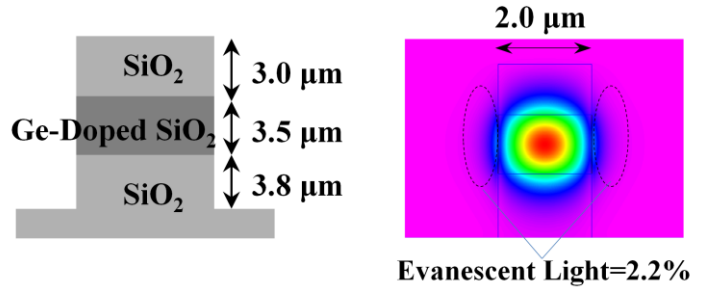

(a)

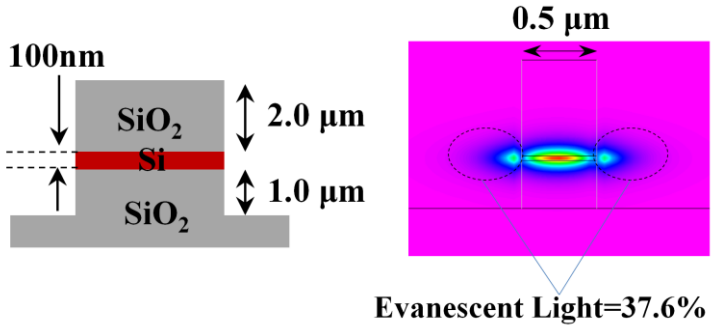

(b)

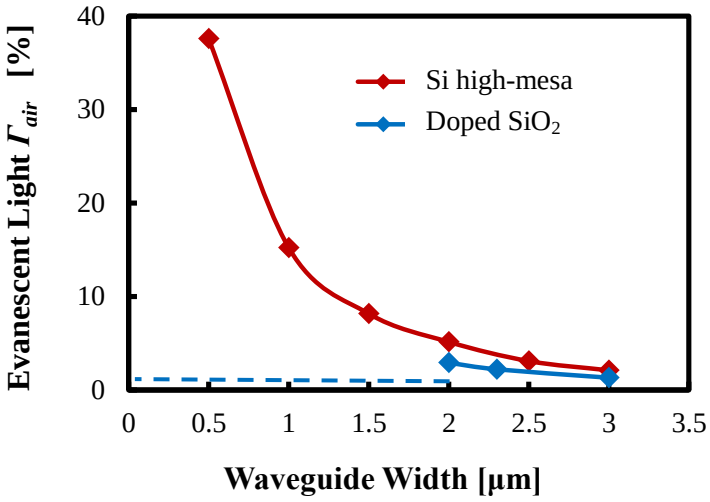

(c)

Fig. 3.2. Cross-section and fundamental TE modal pattern in (a) Previous SiO_2 high-mesa waveguide [17] and (b) 100 nm-thick Si high-mesa waveguide designed in this work; (c) A comparison of evanescent light Γ_{air} of SiO_2 and Si high-mesa waveguides at different widths.

3.3 Silicon high-mesa waveguide fabrication

Based on the design above, Si high-mesa waveguides were fabricated on commercial available silicon-on-insulator (SOI) substrate with a top Si layer of 100 nm and a buried oxide (BOX) layer of 3 μm. The thick oxide layer serves to optically isolate the waveguide from the high refractive index Si substrate, eliminating loss due to substrate leakage. In the proposed high-mesa structure the Si-core is sandwiched by two SiO_2 layers both on the top and at the bottom. Hence, a 2 μm-thick SiO_2 layer was deposited on the substrate via low pressure chemical vapor deposition to act as a top cladding for protecting the waveguide from the dust or impurities in air (as shown in Fig. 3.3(a)). A typical cleaning process was performed by washing the substrate in methanol, acetone and isopropanol (in this order) in an ultrasonic bath for five minutes each, followed by a rinse in deionized water. Subsequently, the substrate was coated with e-beam resist and exposed by electron beam lithography (as shown in Fig. 3.3(b)). After development, the designed waveguide patterns were generated in the e-beam resist and the patterned e-beam resist provided a mask for the next etching step. The substrate was then etched in an inductively coupled plasma (ICP) etching machine to generate high-mesa

waveguides by CHF_3 gas (as shown in Fig. 3.3(c)). The SEM image of the fabricated 1 μm-wide waveguide is shown in Fig. 3 (d). It looks that the waveguide has a relatively vertical and smooth sidewall. The fabrication process has significant impact on the scattering loss and absorption loss of the waveguide, the following sections will discuss fabrication induced optical loss and the technique to reduce the propagation loss.

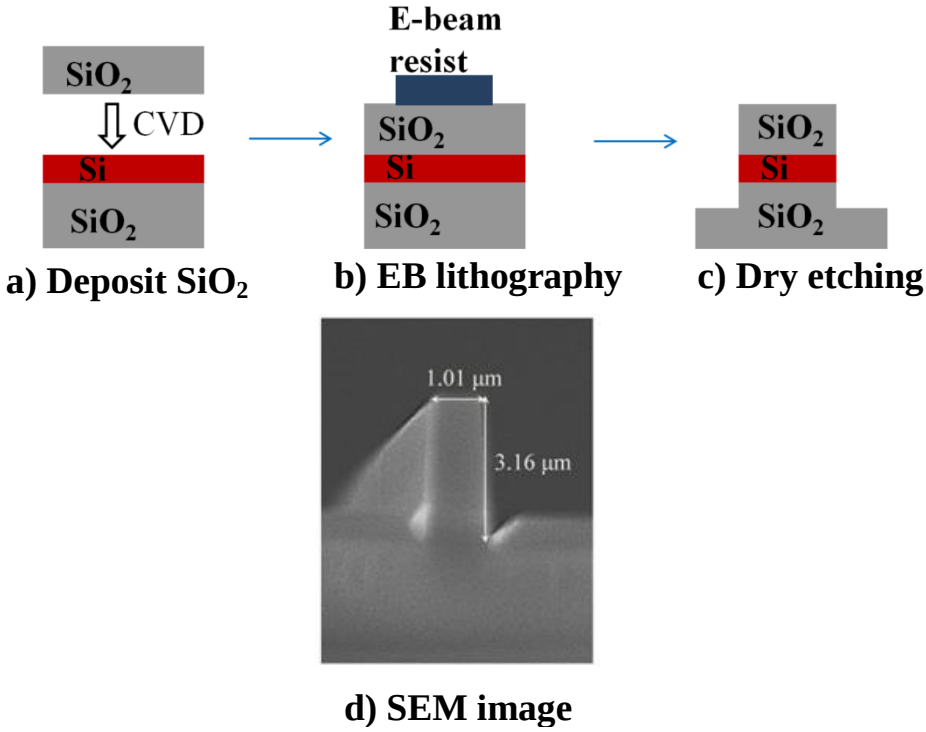

Fig. 3.3. Fabrication process of the Si high-mesa waveguide (a)-(c), and (d) SEM image of the fabricated 1 μm-wide waveguide.

3.4 Propagation loss measurement and analysis

The propagation loss α was evaluated by using Fabry–Perot interferometric method [25]. This method requires an excitation of the waveguide with a broadband amplified spontaneous emission source. Therefore, light from a distributed feedback (DFB) laser source was coupled into the waveguide in TE mode through a polarization-maintaining lensed fiber. The temperature of the DFB laser became higher with the increased input power (current). The peak of the optical feedback changes with the temperature, so that the wavelength of the DFB laser moves to the longer wavelengths. As a sequence, we can obtain a broadband laser source by using the DFB laser. A polarizer was used to align the input light polarization between the laser and the fiber. Output optical power of the waveguide is collected using a photo-detector and the detected data were recorded automatically in a computer. At last, α was evaluated by curve fitting to account for the change of input power [25]. Based on the simulation, the waveguide is becoming multi-mode when the width is $\geqslant$2 μm. Though the waveguide is multi-mode, we can align the coupling fiber to excite only 0th mode of the waveguide [26]. Taking into account that the

uncertainty from the laser and photo-detector, the upper limit of the error in the loss measurement is estimated to be < 8%.

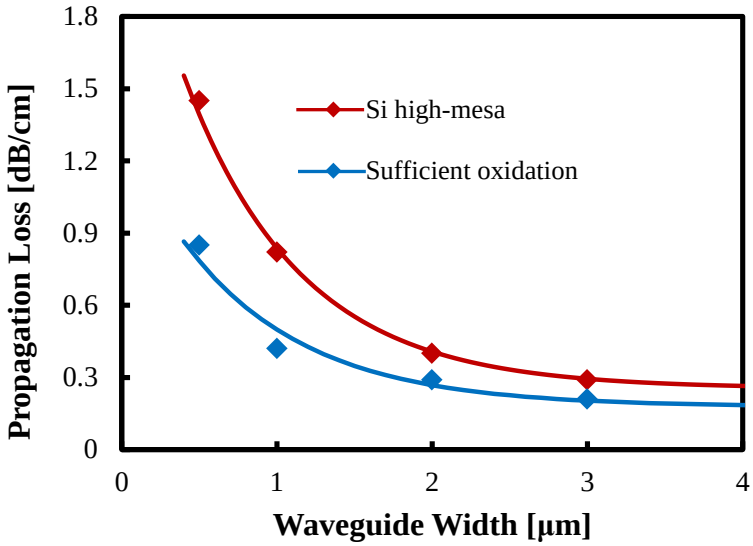

(a)

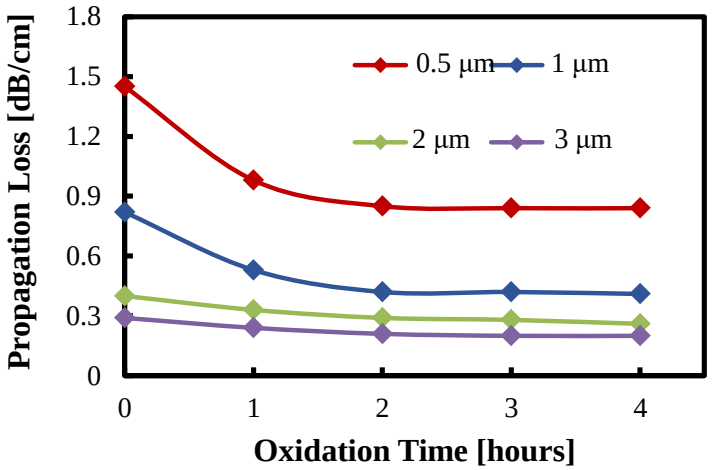

(b)

Fig. 3.4. Measured propagation loss of the Si high-mesa waveguides (a) Before and after sufficient oxidation, and (b) Propagation loss of the 0.5-3 μm-wide waveguides with different oxidation time

The evaluated α is shown in Fig. 3.4(a) as a function of the waveguide width. The measured α of the just-fabricated 100 nm Si waveguides is still much higher than the required 0.05 dB/cm [18]. The propagation loss of a waveguide is generally attributed to three different mechanisms: radiation loss, absorption loss and scattering loss. The simulated TE mode at the wavelength of 1550 nm shown in Fig. 3.2(b) indicates that the optical field is well-confined in the waveguide without any leakage to the substrate. In addition, the materials of the waveguide, Si and SiO_2, are highly transparent around 1550 nm. In addition, a low power laser was used in the measurement, so the loss caused by the nonlinear effect of Si should be negligible. According to our simulation by BPM, the optical loss is also negligible when the sidewall of the waveguide is a little titled. As a result, the main causes of α in our case are the scattering loss α_s from the rough sidewall [26, 27] and the absorption loss α_a from damaged Si caused by the ICP etching [28]. Oxidation of Si has been shown to be effective at reducing the sidewall scattering and recovering the damaged Si, and has been successfully employed by several studies [26, 27]. After oxidation, a thin Si layer near the sidewall is oxidized into SiO_2, so the damaged Si is recovered. The α_a from damaged Si is reduced due to the transformation to SiO_2.

Meanwhile, the sidewall roughness is also reduced after oxidation. According to the Payne-Lacey model [29], a lower sidewall roughness indicates a lower α_s. Therefore, the reduction of propagation loss by oxidation of Si is imperative to realize our ppm-order detection purpose.

3.5 Further loss reduction and discussions

In order to further reduce the propagation loss, thermal oxidation technique was applied to the Si high-mesa waveguides. For the oxidation, the waveguides were placed in a ceramic boat and loaded at one end of a quartz tube furnace. Once the samples were loaded, the tube was closed at both ends using rubber gasket-loaded threaded steel end caps. O_2:N_2=1:4 (mole ratio) gas flow was established in the tube for a few minutes to ensure that it was full of stable O_2 and N_2. The flow rate was controlled by a flow controller, so that a nominal 700 standard cubic centimeter per minute (sccm) flow rate was maintained. The temperature of the furnace was raised to the oxidation temperature of 1000 ℃ at the rate of approximately 1 ℃/sec. Once the target temperature was reached, it was kept differently from 1 to 4 hours for testing the effect of thermal oxidation condition on the reduction of the propagation loss.

After 2 hours sufficient oxidation, as shown in Fig. 3.4(a), α is effectively reduced from 1.45 to 0.85 dB/cm for width=0.5 μm and from 0.29 to 0.21 dB/cm for width=3μm, which follows our above analysis of the oxidation of Si. As shown in Fig. 3.4(b), longer time oxidation (≥ 2 hours) does not induce obvious further reduction of α, which is attributed to the formation of SiO_2 preventing oxygen from diffusing through the grown oxide film into the Si [30].

As discussed above, the propagation loss α of the 100 nm thick Si high-mesa waveguide is due to the scattering loss α_s and the absorption loss α_a ($\alpha=\alpha_s+\alpha_a$). Therefore, we concentrate in the following on the influences of α_s and α_a to α in the waveguide before oxidation and sufficient oxidation. α_s is given by the Payne-Lacey model [29]:

$$\alpha_s \propto \frac{\sigma^2 \Gamma_{air}}{(\frac{w}{2})^2} \qquad (1)$$

where σ is sidewall roughness and w the waveguide width. In order to clarify the affection of oxide layer on the evanescent light Γ_{air}, Γ_{air} was calculated theoretically. Once SiO_2 grows to a thickness of approximately 20 nm, the Si oxidation ceases to be the fast reaction and becomes a quite slow diffusion limited process [31]. Even after sufficiently long-time oxidation (>10

hours), the saturated SiO_2 is thinner than 100 nm because SiO_2 formation acts as a diffusion barrier and hinders further oxidation. Therefore, the largest thickness of the formed SiO_2 at the sidewall is reasonable to be supposed as 100 nm. Figure 3.5 shows the difference of Γ_{air} with different SiO_2 thickness of the waveguide side-wall from 0 - 100 nm when the waveguide is 0.5 - 3 μm-wide. From the results, we can see that the difference of Γ_{air} is only 0.54% with a 100 nm thick oxidation layer. For wider waveguides, the difference of Γ_{air} is less than 0.2%. This little change indicates that the oxidation process has negligible affection on Γ_{air}.

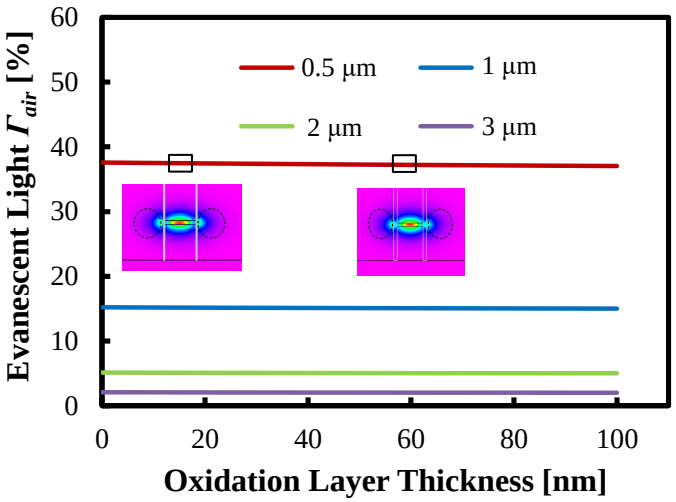

Fig. 3.5. Calculated evanescent light Γ_{air} change versus different oxidized sidewall SiO_2 thickness (Inserts: TE mode patterns when the oxidation layer thickness=20 and 60 nm for 0.5 μm-wide)

As the oxide layer has negligible affection on Γ_{air}, based on Eq. 1, α_s is from the reduced sidewall roughness. α_s was calculated by using Payne-Lacey model under different side-wall roughness until the trend of the calculated α_s curve is closest to that of the measured α. In Paune-Lacey method, showed that for accurate loss calculations, it is necessary to take into account correlation length. In our case, the correlation length is estimated from the SEM image of the waveguide sidewall. The obtained correlation length is ～98 nm. Figure 3.6 shows the calculated α_s curves which corresponding to 18 and 12 nm side-wall roughness σ for the before oxidation and 4 hours oxidized waveguide, respectively. Scattering loss is significantly reduced from 1.14 to 0.58 dB/cm when the waveguide width is 0.5 μm. From Eq. 1, α_s is zero when w $\rightarrow\infty$. Considering $\alpha=\alpha_s+\alpha_a$, the loss difference of the fitted α curve when w $\rightarrow\infty$ is considered to be the reduced absorption loss $\Delta\alpha_a$, which is 0.07 dB/cm. The reduction of both α_s and α_a verifies that thermal oxidation technique effectively reduces the sidewall roughness and recovers damaged Si. “Removing oxidation layer and thermal oxidation again” is an effective method of further reducing the propagation loss. Actually, we also noticed that this method has been applied in Si waveguide

loss reduction [16]. In our case, the obtained 0.4 dB/cm loss has satisfied the requirement of breath sensing demand. So, we did not try “Removing oxidation layer and thermal oxidation again”. In future, we may try to use this method if the loss is required to be lower.

As mentioned in Ref. 18, ppm-order detection requires the propagation loss ≤ 0.05 dB/cm and Γ_{air}≥10%. The Γ_{air} of 0.5 and 1 μm–wide waveguide fully satisfies the requirement. Though the propagation loss has been significantly reduced, further reduction is still needed in realizing ≤ 0.05 dB/cm. The effective thermal oxidation technique confirmed in this work will drive further loss reduction to the required level. For example, employ thermal oxidation technique plus wet-etching SiO_2 [27]. As a result, CRDS based on the Si high-mesa waveguides is expected to sense ppm-order breath content for health-monitoring.

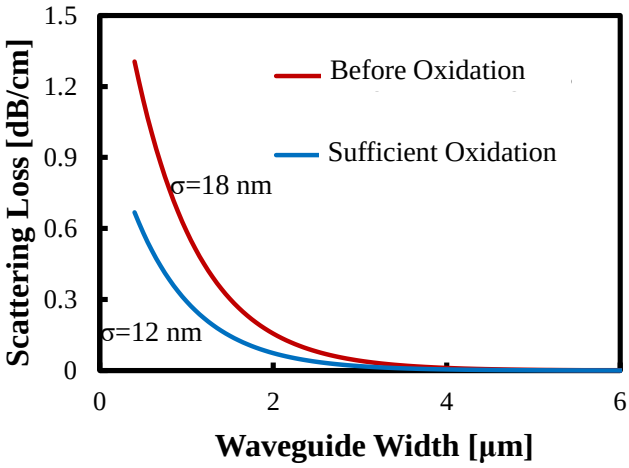

Fig. 3.6. Theoretically calculated scattering loss α_s curves according to the trend of the measured α.

3.6 Conclusions

In this work, we have designed and fabricated 100 nm-thick Si core high-mesa waveguides for CRDS breath sensing. Compared with previous SiO_2 high-mesa waveguides, Si waveguides show a much higher Γ_{air}, which enables a possibility of a ppm-oder CRDS. The just-fabricated waveguide has a relatively high α, which is caused by α_s and α_a. By using thermal oxidation, part of the damaged Si is recovered and the sidewall roughness is reduced. As a result, an obvious reduction of α has been achieved. In future work, α_s and α_a will be further reduced and the waveguides may be applied in CRDS photonic circuits.

3.7 References

[1] United Nations Population Division, World Population Ageing 2017 United Nations population division, http://un.org/en/development/desa/population/theme/ageing/WPA2017.shtml.

[2] T. Huynh and H. Haick, “Autonomous Flexible Sensors for Health Monitoring,” Adv. Mater. **30**, 1802337 (2018).

[3] T. H. Risby and S. F. Solga, “Current status of clinical breath analysis,” Appl. Phys. B **85**, 421-426 (2006).

[4] B. Timmer, W. Othuis, and A. Berg, “Ammonia sensors and their applications - A review,” Sensor Actuat. B-Chem.**107**, 666-677 (2005).

[5] G. Peng, U. Tisch, O. Adams, M. Hakim, N. Shehada, Y. Y. Broza, S. Billan, R. Bortnyak, A. Kuten, and H. Haick, “Diagnosing lung cancer in exhaled breath using gold nanoparticles,” Nat. Nanotechnol. **4**, 669-673 (2009).

[6] C. L. Dai, “A capacitive humidity sensor integrated with micro heater and ring oscillator circuit fabricated by CMOS-MEMS technique,” Sens. Actuators B Chem. **122**, 375-380 (2007).

[7] H. Bi, K. Yin, X. Xie, J. Ji, S. Wan, L. Sun, M. Terrones, and M. S. Dresselhaus, “Ultrahigh humidity sensitivity of graphene oxide,” Sci. Rep. **3**, 2714 (2013).

[8] J. Weremczuk, G. Tarapata, and R. Jachowicz “Humidity sensor printed on textile with use of ink-jet technology,” Procedia Eng. **47**, 1366-1369 (2012).

[9] M. K. Sofian, O. Kadri, I. Yousef, and M. Kanan, “Semiconducting metal oxide based sensors for selective gas pollutant detection,” Sensors **9**, 8158–8196 (2009).

[10] N. Yamazoe, and K. Shimanoe, “Theory of power laws for semiconductor gas sensors,” Sens. Actuators B **128**, 566–573 (2002).

[11] F. Berger, J. Baptiste, and S. Heintz, “Detection of hydrogen fluoride using SnO_2-based gas sensors: Understanding of the reactional mechanism,” Sens. Actuators B. **143**, 152–157 (2009).

[12] G. Berden and G. Meijer, “Cavity ring-down spectroscopy: Experimental schemes and applications,” Int. Rev. Phys. Chem. **19**, 565-607 (2000).

[13] J. Manne, O. Sukhorukov, W. Jager, and J. Tulip, “Pulsed quantum cascade laser-based cavity ring-down spectroscopy for ammonia detection in breath,” Appl. Opt. **45**, 9230–9237 (2006).

[14] M. Mazurenka, A. Orr-Ewing, R. Peverall, and G. Ritchieb, “Cavity ring-down and cavity enhanced spectroscopy using diode lasers,” Annu. Rep. Prog. Chem. C **101**, 100–42 (2005).

[15] J. B. Dudek, P. Tarsa, A. Velasquez, M. Wladyslawski, P. Rabinowitz, and K. Lehmann, “Trace moisture detection using continuous-wave

cavity ring-down spectroscopy," Anal. Chem. **75**, 4599–605 (2003).

[16] H. Abe and K. Yamada, "Performance evaluation of a trace-moisture analyzer based on cavity ring-down spectroscopy: direct comparison with the NMIJ trace- moisture standard," Sens. Actuators A **165**, 230 (2011).

[17] J. Chen, H. Hokazono, D. Nakashima, M. Tsujino, Y. Hashizume, M. Itoh, and K. Hamamoto, "Low loss silica high-mesa waveguide for infrared sensing," Jpn. J. Appl. Phys. **53**, 022502 (2014).

[18] H. Hokazono, W. Li, S. Enami, H. Jiang, and K. Hamamoto, "Gas sensing demonstration by using silica high-mesa waveguide with amplified cavity ring down spectroscopy technique," IEICE Electron. Expr. **15**, 1-8 (2015).

[19] W. Li, Y. Han, Z. Chen, H. Jiang, and K. Hamamoto, "Amplifier-assisted CRDS (cavity ring-down spectroscopy) toward compact breath sensing," Jpn. J. Appl. Phys. **58**, SJJD01 (2019).

[20] D. Nakashima and K. Hamamoto, "Proposal of Novel Strip High-Mesa Waveguide for Infrared Absorption Sensing," Appl. Phys. Express **5**, 062202 (2012).

[21] A. Intekhab, "SOI-based Si/SiO_2 High-mesa Waveguide for Optical Absorption Sensing," Thesis, Kyushu Univ. (2013).

[22] J. Chen, H. Hokazono, D. Nakashima, M. Tsujino, Y. Hashizume, M. Itoh, and K. Hamamoto, "Proposal of multi-slot silica high-mesa

waveguide for infrared absorption," IEICE Electron. Expr. **10**, 1-7 (2013).

[23] S. Yano, K. Kameyama, and K. Hamamoto, "Low Loss SOI-Based High-Mesa Waveguides Fabricated Using Neutral Loop Discharge (NLD) Plasma Etching for Compact Breath-Sensing System," Integrated Photonics and Nanophotonics Research and Applications (IPNRA) (2007).

[24] I. Alam, and K. Hamamoto, "Slot waveguide by using double high-mesa structure for optical absorption sensing," Jpn. J. Appl. Phys. **49**, 122503 (2010).

[25] S. Taebi, M. Khorasaninejad, and S. Saini, "Modified Fabry-Perot interferometric method for waveguide loss measurement," Appl. Opt. **47**, 6625–6630 (2008).

[26] K. K. Lee, D. Lim, L. C. Kimerling, J. Shin, and F. Cerrina "Fabrication of ultralow-loss Si/SiO_2 waveguides by roughness reduction," Opt. Lett. **26**, 1888–1890 (2001).

[27] D. K. Sparacin, S. J. Spector, and L. C. Kimerling, "Silicon waveguide sidewall smoothing by wet chemical oxidation," IEEE J. Lightwave Technol. **23**, 2455–2461 (2005).

[28] A. Yahata, S. Urano, T. Inoue, and T. Shinohe, "Smoothing of Si trench sidewall surface by chemical dry etching and sacrificial oxidation," Jpn. J. Appl. Phys. **37**, 7 (1998).

[29] F. P. Payne and J. P. R. Lacey, “A theoretical analysis of scattering loss from planar optical waveguides,” Opt. and Quantum Electron. **26**, 977-986 (1994).

[30] M. Liu, P. Jin, Z. Xu, D. Hanaor, T. Gan, and C. Chen , “Two-dimensional modeling of the self-limiting oxidation in silicon and tungsten nanowires,” Theor. Appl. Mech. Lett. **6**, 195–199 (2016).

[31] J. T. Wright, D. Carbaugh, M. Haggerty, A. Richard, D. Ingram, S. Kaya, W. Jadwisienczak, and F. Rahman, “Thermal oxidation of silicon in a residual oxygen atmosphere—The RESOX process—For self-limiting growth of thin silicon dioxide films,” Semicond. Sci. Technol. **31**, 105007 (2016).

Chapter 4 Asymmetric-ration optical power couplers based on nano-pixel structure

4.1 Introductory overview

Photonic integrated circuits (PICs) based on a silicon (Si) platform have attracted tremendous interest for constructing efficient optical devices and systems due to high refractive index contrast and complementary metal-oxide-semiconductor compatibility [1-5]. In the development of PICs, a compact optical power coupler is one of the key components due to the requirements of power distribution among its building blocks [6-10]. As mentioned in Chapter 1.5, symmetric couplers have been studied to some extent in the past. In contrast, it is difficult to design asymmetric optical power couplers by using traditional Y-branch waveguides, directional couplers or MMI waveguides [11-16].

In this chapter, two asymmetric couplers with a splitting power ratio of 1:9 and 1:99 have been designed via deep learning method. To realize the asymmetric ratios, the coupler

region was divided into discrete nano-pixels in the shape of circular holes with the same dimension. Deep learning was utilized to decide the material of each hole to be waveguide or air one by one and FDTD simulation was introduced to evaluate the performance of the designed couplers. The splitting power ratio of 1:9.007 and 1:99.004 has been realized in the two couplers with a same footprint of $3.4 \times 3.2\ \mu m^2$. In addition, the positions and widths of the output waveguides were further optimized as the excess loss of the designed coupler is a bit high of more than 3.50 dB. Through the optimization of the configuration, a scattering loss reduction of 1.7 dB by position optimization, and a coupling loss reduction of 1.6 dB by width widening were confirmed. The achieved design exhibited a operation wavelength from 1500-1600 nm and a sufficient fabrication tolerance of ± 10 nm ($\pm 11\%$).

4.2 Deep learning designed optical power couplers

As shown in Fig. 4.1(a), the optical coupler consists of two sections: input/output waveguides and coupler section. The coupler section is composed of discrete nano-pixels in the shape of circular holes with the same dimension. The widths of the input/output waveguides are initially set as 0.5 μm to ensure the

single-mode condition around the wavelength of 1550 nm.

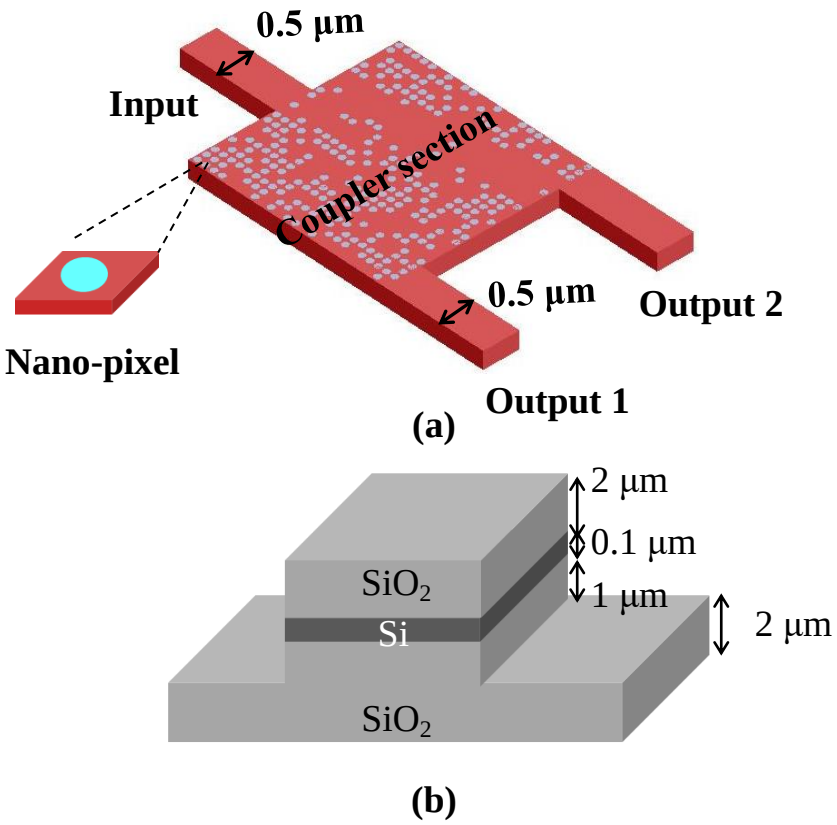

Fig. 4.1 Optical power couplers: (a) Schematic diagram: input light is divided into two output waveguides by the coupler and (b) 100 nm Si high-mesa waveguide cross-section.

The couplers are constructed on the Si high-mesa waveguide [17] as shown in Fig. 4.1(b). The waveguide is based on a silicon-on-insulator wafer with a device layer of 100 nm, a top SiO_2 cladding of 2 µm and a bottom SiO_2 cladding of 3 µm. The bottom cladding is etched with a thickness of 1 µm. In our previous work [17], we have demonstrated that the fabrication of the waveguide was able to be completed in single step

etching process and the propagation loss of the waveguide was as low as 0.2 dB/cm.

When a light encounters an optical structure with an inhomogeneous refractive index distribution along its path, it undergoes reflection, refraction and scattering. The goal of our nanostructured pixel power coupler is to organize the optical interaction events, such that the overall effect of the reflection, refraction and scattering guides the beam to the output port with desired splitting power ratio. To design the 1:9 and 1:99 couplers, we designed nano-pixel structure based on deep learning with three layer deep neural network (DNN) [18-25]. The DNN process is described as follows:

(1) Preparation of the training dataset for supervised DNN learning

We used the Rsoft simulation package (Rsoft Photonics CAD Suite: 9-33B7B8C7) to generate training data. Our input data were several 24 × 24 pixel vectors (HVs), each labeled with its corresponding splitting power ratio. Each pixel consists of a circular with an identical diameter of 90 nm either as the binary state of 1 for occupied by air ($n=n_{air}$) or 0 for pristine ($n=n_{waveguide}$). Changing the refractive index at a hole position modifies the local effective index inside of the coupler and

change the propagation path for the light in the device. Afterward, 5000 randomly fluctuated nano-pixel structure patterns were generated and exported using Python automation. Next, each nano-pixel structure pattern was imported into the Rsoft simulation package to make a FDTD simulation and collect the corresponding splitting power ratio. The data contained 5000 numerical simulations, and thus, we used the relationships between the nano-pixel structure patterns and the splitting power ratio values of the 5000 prepared structures to label the training data for supervised learning.

(2) Training of DNN

We fed the DNN with the output from the numerical optical experiments and trained it to represent the relationship between the HVs and the splitting power ratio. It is known that 9:1 is better portion for training over test data-set among 5000 patterns [26], therefore, we choose 9:1. Training was terminated after a fixed number of iterations to ensure convergence. Finally, the predicted splitting power ratio was entered and the corresponding HVs were exported by the DNN model via the inverse design process [18-25]. Therefore, we obtained the optimal pattern of nano-pixels for the target splitting power ratio via the DNN model. The objective of the optimization is to find

the structures that satisfy the required splitting power ratio (1:9 and 1:99 in our case) with an excess loss α (α < 0.5 dB in our case) and a broadband performance from 1500-1600 nm. Here, α is the total loss between input waveguide and output waveguides.

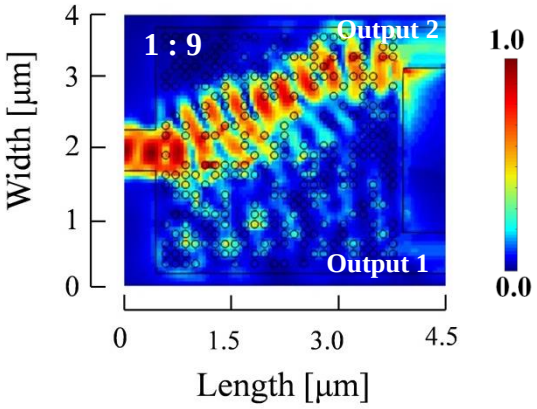

Fig. 4.2 DNN design result of 1:9 coupler in the 3.4 × 3.2 μm^2 coupler area

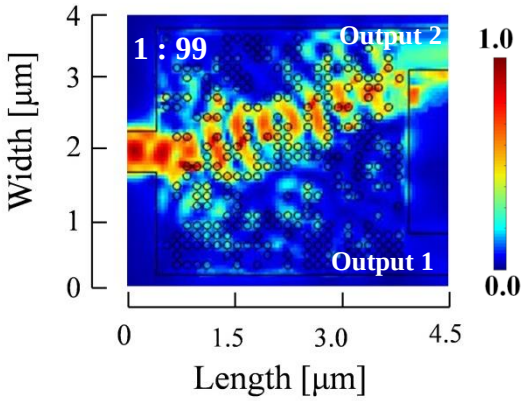

Fig. 4.3 DNN design result of 1:99 coupler in the 3.4 × 3.2 μm^2 coupler area

The finally optimized couplers have a footprint of 3.4 × 3.2 μm^2. There are totally 576 pixels consisting of circular air holes with an identical diameter of 90 nm randomly located in the

coupler area. Figure 4.2 and 4.3 show the simulated optical fields in the 1:9 and 1:99 coupler, respectively. The color bar at the right side of the simulated results indicates the normalized light intensity profile, where different color stands for different light intensity, for example the dark blue means no light. The above results verify that the 1:9 and 1:99 couplers have been successfully realized by using the deep learning method, which overcomes the difficulty that there is less matured design-theory for asymmetric couplers.

4.3 Analysis and Reduction of the Excess Loss

For the 1:9 and 1:99 coupler as shown in Fig. 4.2 and 4.3, the estimated α were 3.7 and 3.62 dB, respectively at the wavelength of 1550 nm, which are higher than our target (α<0.5 dB). It is therefore necessary to carried out analysis and reduction of α for future applications in photonic integrated circuits. For the light coupling between two optical waveguides, mismatch of the waveguide center and the model field usually lead to a high optical loss [28]. In our case, we can see that the optical field at the edge of the optical coupler section is obviously larger than the width of the output waveguide (0.5 μm). This will cause a serious mismatch of the waveguide center

and the model field, which is the main reason of the excess loss.

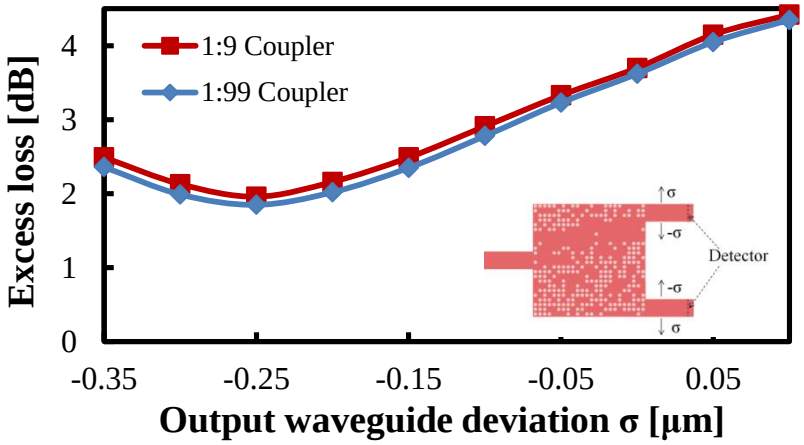

(a)

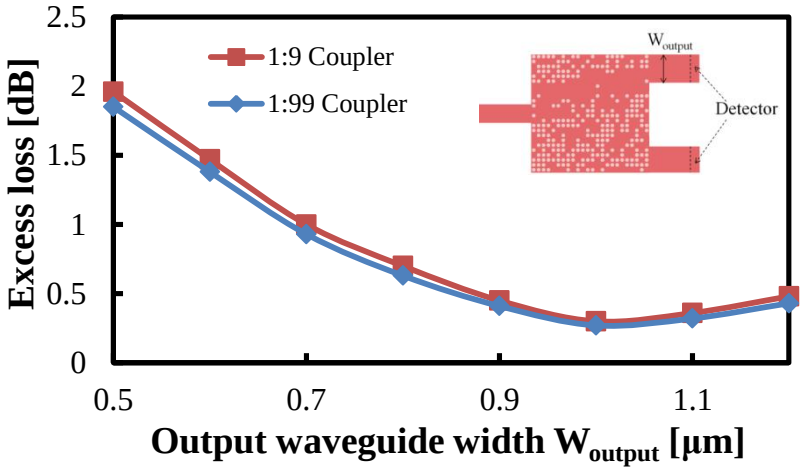

(b)

Fig. 4.4 Influence of the waveguide widths and locations on the excess loss: (a) Excess loss at different waveguide locations (insets show the schematics of the simulation) and (b) Output waveguide widths versus excess loss.

In order to reduce α, the positions and widths of the output waveguides are optimized for the two couplers. Figure 4.4 (a) shows the influence of the 0.5 μm wide output waveguide

locations on the excess loss. The deviation σ is defined as σ > 0 for an outward deviation and Δ < 0 an inward deviation (as shown in the inset of Fig. 4.4 (a)). In the simulation, the width of the input waveguide is W_{input} = 0.5 μm and the detector locates at the edges of the two output waveguides. From the simulated results, we can see that σ = -0.25 μm is the best location for the 1:9 and 1:99 couplers and α has a reduction of 1.7 dB compared with the original position σ = 0 μm. α with different output waveguide width W_{outpu} is examined as shown in Fig. 4.4 (b). The results indicate the optimized W_{output} = 1 μm for both 1:9 and 1:99 couplers. After the width optimization, α has a further decrease of 1.6 dB at the wavelength of 1550 nm for the both couplers. The significant α reduction reveals that the waveguide centers and model fields between the output waveguide and the coupler section have been matched each other much better.

Figure 4.5 (a) and (b) show a comparison of the calculated excess loss α for the output waveguides with a width of 0.5 and 1 μm from the wavelength 1500 nm to 1600 nm. The reduction of α (Δα) is 3.4 and 3.35 dB for the 1:9 and 1:99 coupler at the wavelength of 1550 nm, respectively. The reduction of α indicates that the optimization of the output waveguide positions

and widths is effective to improve the coupling efficiency between the coupler section and the output waveguides.

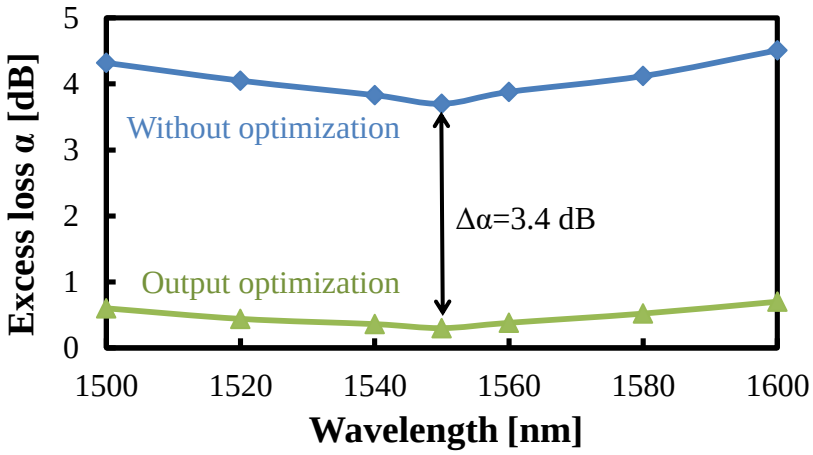

(a)

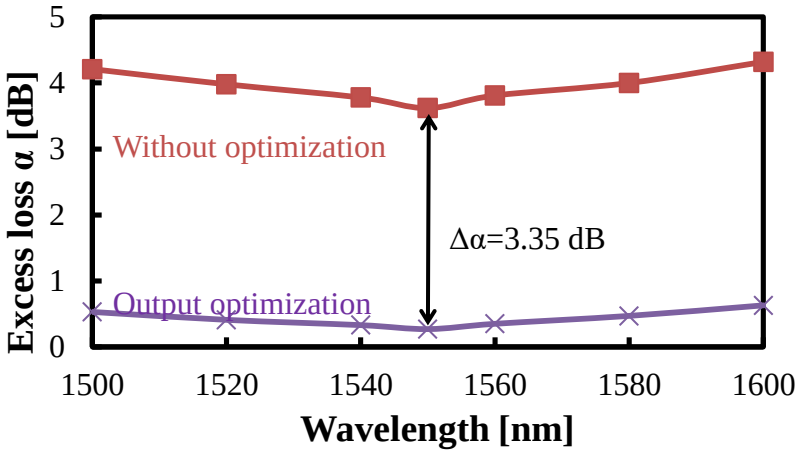

(b)

Fig. 4.5 Comparison of the excess loss as the output waveguide with a width of 0.5μm and 1 μm, (a) 1:9 coupler and (b) 1: 99 coupler.

4.4 Input/ output waveguide geometry unification

The widths of the input and output waveguides after the loss reduction are different from each other, which are 0.5 and 1μm

respectively. In order to match waveguide width and benefit for future application, we design a mode size converter also based on deep learning designed nano-pixel structure. To be brief, we do not give the details of the simulation and calculation. The design process is similar to that of the above design of the optical power coupler. The finally optimized device is shown in Fig. 4.6, which consists of the optical power coupler and the mode converter. The mode converter occupies a space of 1 × 2 μm^2, which is much more compact compared with the traditional tapered waveguides. There are 74 holes with an identical diameter of 90 nm randomly located in the mode converter.

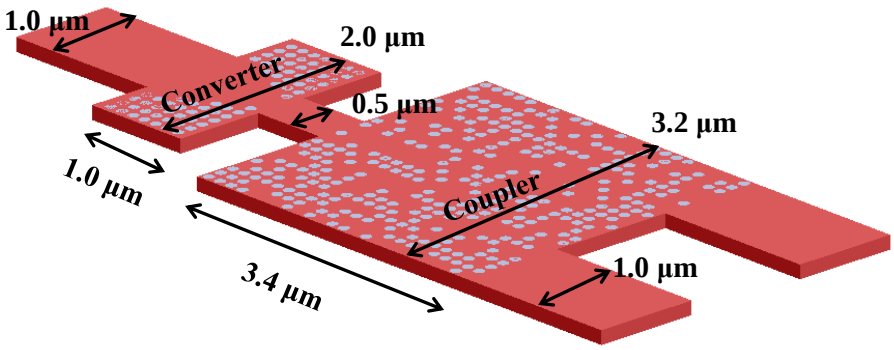

Fig. 4.6 Schematic of the coupler after adding a mode converter to match the input and output waveguide

Figures 4.7 shows the simulated optical filed in the device with a splitting ratio of 1 (output 1) : 9.006 (output 2) at the wavelength of 1550 nm. The color bar at the right side of the

simulated results indicates the normalized light intensity profile, where different color stands for different light intensity. In the device, the light propagated in the 1 μm-wide waveguide firstly enters into the 1 × 2 μm^2 mode converter, which in turn gradually becomes narrow in order to be coupled into the 500 nm-wide waveguide. Compared with the 1 μm-wide waveguide, the light intensity is enhanced in the 500 nm-wide waveguide, which is because the area of confining light is smaller. Subsequently, the light from the 500 nm-wide waveguide is launched into the optical power coupler based on nano-pixel structures. The inversely designed optical power coupler as described in section 2 gradually divides the light into two beams and finally transforms it into 1:9.006 in the output waveguides.

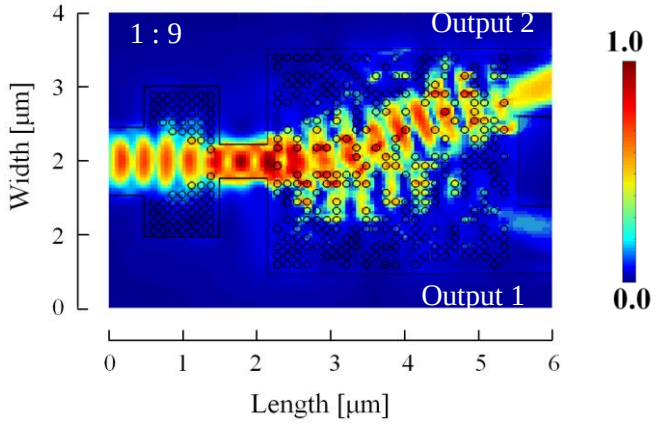

Fig. 4.7 Simulated light propagation in the 1:9 coupler at the wavelength of 1550 nm

The coupler with a splitting power ratio as 1:99.003 is shown

in Fig. 4.8 by using the same mode converter and just modifying the positions of the nano-pixels in the coupler section. This result verifies that flexible splitting ratios are realized in the same area just through optimizing positions of the nano-holes.

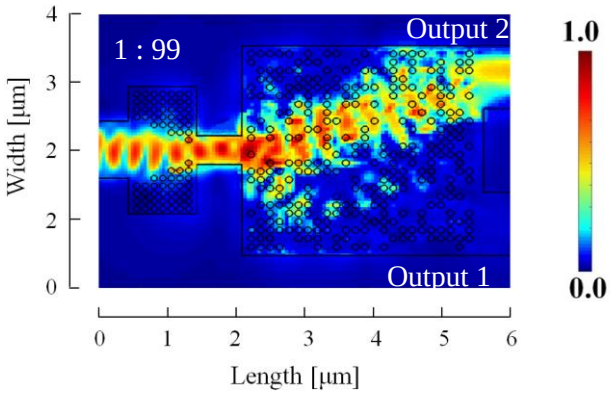

Fig. 4.8 In the same area, 1 (output 1) : 99 (output 2) beam splitter is realized by modifying the positions of the nano-piexls.

4.5. Performance of optical power couplers

For a nano-photonic device, there are two general requirements to be fulfilled to easily fabricate the device: alignment/etching steps and fabrication tolerance [29, 30]. In our designed beam couplers, the waveguide and holes are with the same etching thickness, so the device is able to be fabricated in only single-step etching procedure. The single-step etching avoids critical and complex alignments in electro-beam or photolithography, improving the accuracy of fabrication. Consequently, the most critical technological parameter with the

largest contribution to the coupler performance is the sizes of the holes.

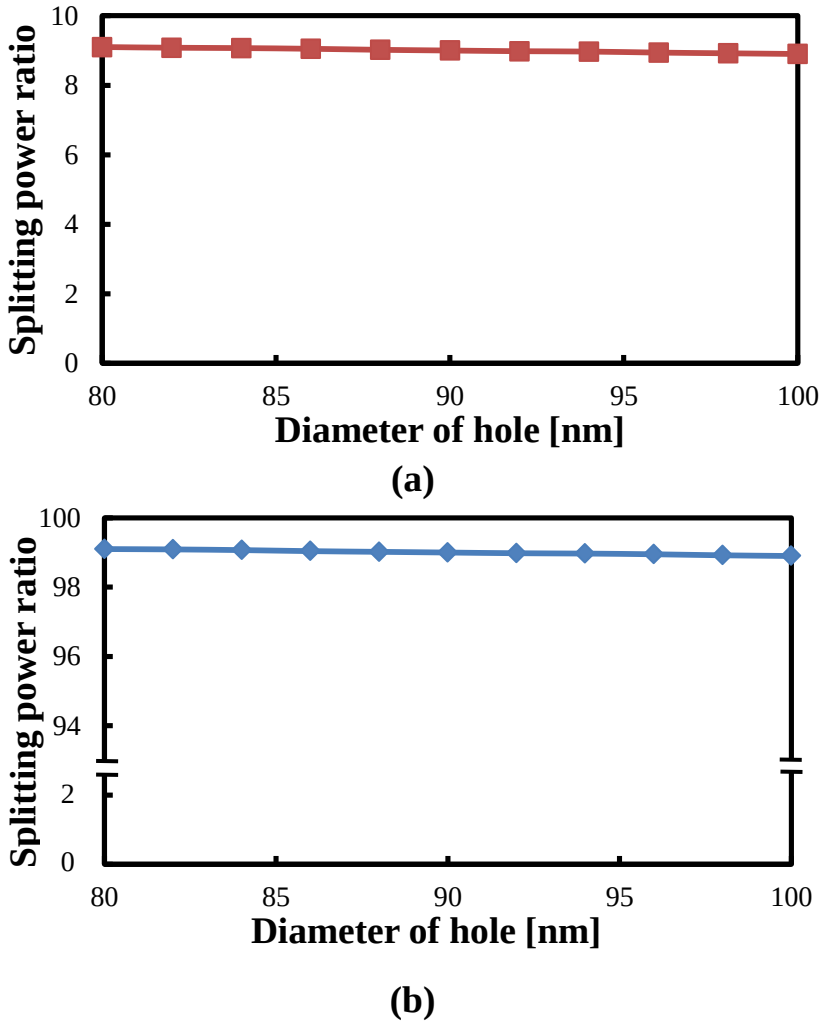

Fig. 4.9 Calculated split power ratio versus hole diameter (a) 1: 9 and (b) 1:99 coupler, which predicts excellent robustness of the device against fabrication imperfection.

The influence of the diameter on the splitting ratio has been calculated. For our devices, it is able to be fabricated by using electron-beam lithography with a resolution as high as sub-10 nm. Considering this resolution, the diameter has been varied

with a tolerance of ± 10 nm (± 11%) in the calculation, while keeping the other parameters constant. Figure 4.9 shows the calculated split power ratio with different diameters. We can see that the variation of the splitting ratio is sufficiently low with a tolerance of ±10 nm (±11%). The splitting ratio is 1:99.1 and 1:9.1 at the diameter of 80 nm, and 1:98.9 and 1:8.9 at 100 nm. The insensitivity of the splitting ratio performance to the diameters of the holes predicts excellent robustness of the device against fabrication imperfection.

Another important factor for the couplers application is wavelength dependent performance shift. Figure 4.10 (a) and (b) show the splitting ratio of the two couplers from 1500-1600 nm, which indicates that the device has a quite low wavelength dependent performance shift in the range of 1500-1600 nm. Figure 4.10 (c) exhibits the relationship of the excess loss α and working wavelength. Though α increases when the wavelength deviates the optimum value of 1550 nm, it still keeps < 0.8 dB at this broad wavelength range. The wavelength independent performance proves a broadband application in future integrated photonic circuits.

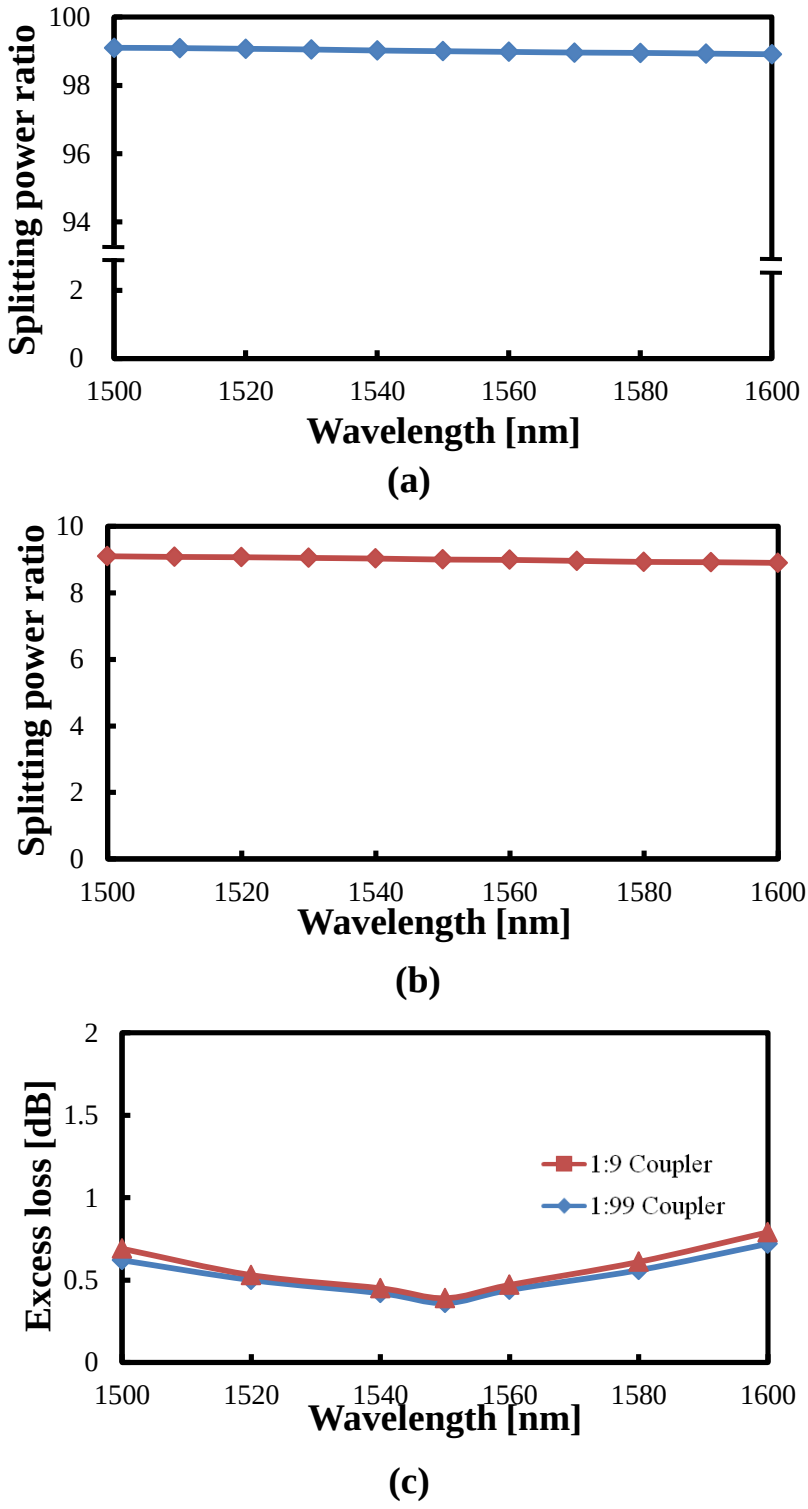

Fig. 4.10 Wavelength dependent device performance: Calculated split ratio versus wavelength for the (a) 1:9 and (b) 1:99 coupler, and (c) Excess loss versus wavelength.

Though the optical power coupler exhibits a broadband application, the bandwidth of the mode converter will also affect the properties of the whole device. We have therefore investigated the excess loss in the mode converter for wavelengths ranging from 1500 to 1600 nm. Here, the excess loss α of the converter is defined as the optical power reduction as the light propagates through the converter. Figure 4.11 shows the calculated α versus wavelength, which predicts that the excess loss is below 0.1 dB for the entire wavelength range. Combining the results of Fig. 4.10 and Fig. 4.11, we can see that the AI assisted inversely designed device including the mode converter and optical power coupler has a wide bandwidth. We also check the fabrication tolerance of the mode converter and just give the obtained results (to be brief). The mode converter possesses the same fabrication tolerance with the coupler, i. e. diameter of the holes ±10 nm.

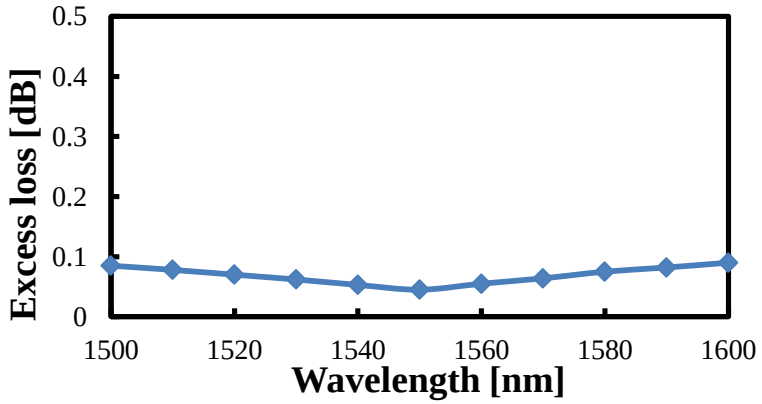

Fig. 4.11 Wavelength dependent α of the mode size converter

4.6. Conclusions

We have designed optical power couplers with a splitting power ratio 1:9 and 1:99. The different ratios are realized via deep learning optimizing nano-pixels. The coupler performance of every trial is evaluated by FDTD method. The optimization of the output waveguide positions and widths was applied to reduce α. After the optimization, α was effectively reduced from 3.7 to 0.3 and 3.62 to 0.27 dB for the1:9 and 1:99 coupler, respectively. In order to enhance the applicability, the output and input waveguides should have the same width, so a mode size converter is designed also via deep learning design at the input side to widen the 0.5 μm -wide waveguide to 1 μm. The converter demonstrates a loss of 0.045dB, a footprint of 1×2 μm^2. The whole devices have an operation wavelength from 1500 to 1600 nm with a fabrication tolerance of ± 10 nm (± 11%).

4.7 References

[1] B. Jalali and S. Fathpour, “Silicon Photonics,” J. Lightwave Technol. 24, 4600 (2006).

[2] L. C. Kimerling, D. Ahn, A. B. Apsel, M. Beals, D. Carothers, Y.-K. Chen, T. Conway, D. M. Gill, M. Grove, C.-Y. Hong, M. Lipson, J. Liu, J. Michel, D. Pan, S. S. Patel, A. T. Pomerene, M. Rasras, D. K. Sparacin, K.-Y. Tu, A. E. White, and C. W. Wong, “Electronic–photonic integrated circuits on the CMOS platform,” Proc. SPIE 6125, 612502 (2006).

[3] R. Takei, Y. Maegami, E. Omoda, Y. Sakakibara, M. Mori, and T. Kamei, “Low-Loss and Low Wavelength-Dependence Vertical Interlayer Transition for 3D Silicon Photonics,” Opt. Express 23(14), 18602–18610 (2015).

[4] D. Thomson, A. Zilkie, J. E. Bowers, T. Komljenovic, G. T. Reed, L. Vivien, D. Marris-Morini, E. Cassan, L. Virot, J. M. Fedeli, J. M. Hartmann, J. H. Schmid, D. X. Xu, F. Boeuf, P. O’Brien, G. Z. Mashanovich, and M. Nedeljkovic, “Roadmap on silicon photonics,” J. Opt. 18(7), 073003 (2016).

[5] G. Reed, G. Mashanovich, F. Gardes, and D. Thomson, “Silicon optical modulators,” Nat. Photonics 4(8), 518–526 (2010).

[6] D. Dai, J. Bauters, and J. E. Bowers, “Passive technologies for future large-scale photonic integrated circuits on silicon: polarization

handling, light non-reciprocity and loss reduction," Light Sci. Appl. 1 , e1 (2012).

[7] Y. Tian, J. Qiu, M. Yu, Z. Huang, Y. Qiao, Z. Dong, and J. Wu "Broadband 1×3 couplers with variable splitting ratio using cascaded step-size MMI," IEEE Photonics J. 10, 6601008 (2018).

[8] Y. Luo, Y. Yu, M. Ye, C. Sun, and X. Zhang, "Integrated dual-mode 3 dB power coupler based on tapered directional coupler," Sci. Rep. 6(1), 23516 (2016).

[9] H. Xu and Y. Shi, "Ultra-broadband dual-mode 3 dB power splitter based on a Y-junction assisted with mode converters," Opt. Lett. 41(21), 5047–5050 (2016).

[10] J. Xing, K. Xiong, H. Xu, Z. Li, X. Xiao, J. Yu, and Y. Yu, "Silicon-on-insulator-based adiabatic splitter with simultaneous tapering of velocity and coupling," Opt. Lett. 38(13), 2221–2223 (2013).

[11] J. D. Love and N. Riesen, "Single-, few-, and multimode Y-junctions," J. Lightwave Technol. 30(3), 304–309 (2012).

[12] W. M. Henry and J. D. Love, "Asymmetric multimode Y-junction splitters," Opt. Quantum Electron. 29, 379–392 (1997).

[13] L. B. Soldano and E. C. M. Pennings, "Optical multi-mode interference devices based on self-imaging: principles and applications," J. Lightwave Technol. 13(4), 615–627 (1995).

[14] E. A. J. Marcatili, “Dielectric rectangular waveguide and directional coupler for integrated optics,” Bell Syst. Tech. J. 48(7), 2071–2102 (1969).

[15] G. F. R. Chen, J. R. Ong, T. Y. L. Ang, S. T. Lim, C. E. Png, and D. T. H. Tan, “Broadband Silicon-On-Insulator directional couplers using a combination of straight and curved waveguide sections,” Sci. Rep. 7(1), 7246 (2017).

[16] Y. Han, W. Li, Z. Hui Chen, H. Jiang, and K. Hamamoto, “Fabrication and analysis of low loss silicon high-mesa waveguides,” Appl. Opt., DOI. 391604 (2020).

[17] W. Li, Y. Han, Z. Chen, H. Jiang, and K. Hamamoto, “Amplifier-assisted CRDS (cavity ring-down spectroscopy) toward compact breath sensing,” Jpn. J. Appl. Phys. 58, SJJD01 (2019).

[18] Y. Liu, W. Sun, H. Xie, N. Zhang, K. Xu, Y. Yao, S. Xiao, Q. Song. “Very sharp adiabatic bends based on an inverse design,” Opt. Lett. 43, 2482-2485 (2018).

[19] A. Michaels and E. Yablonovitch, “Inverse design of near unity efficiency perfectly vertical grating couplers,” Opt. Express 26, 4766–4779 (2018).

[20] B. Shen, P. Wang, R. Polson, and R. Menon, “An integrated-nanophotonics polarization beamsplitter with 2.4 × 2.4 μm2 footprint,” Nat. Photonics 9, 378–382 (2015).

[21] A. Y. Piggott, J. Petykiewicz, L. Su, and J. Vučković, “Fabrication-constrained nanophotonic inverse design,” Sci. Rep. 7, 1786 (2017).

[22] A. Michaels and E. Yablonovitch, “Leveraging continuous material averaging for inverse electromagnetic design,” Opt. Express 26, 31717–31737 (2018).

[23] S. Bhargava and E. Yablonovitch, “Lowering HAMR near-field transducer temperature via inverse electromagnetic design,” IEEE Trans. Magn. 51, 1–7 (2015).

[24] Y. Chen, J. Du, Y. Huang, K. Xu, and Z. He, “Intelligent gain flattening in wavelength and space domain for FMF Raman amplification by machine learning based inverse design, ” Opt. Express 28(8), 11911-11920 (2020).

[25] K. Xu, L. Liu, X. Wen, W. Sun, N. Zhang, N. Yi, S. Sun, S. Xiao, and Q. Song, “Integrated photonic power divider with arbitrary power ratios,” Opt. Lett. 42, 855–858 (2017).

[26] D. Silver, A. Huang, C. J. Maddison, A. Guez, L. Sifre, G. Driessche, J. Schrittwieser, I. Antonoglou, V. Panneershelvam, M. Lanctot, S. Dieleman, D. Grewe, J. Nham, N. Kalchbrenner, I. Sutskever, T. Lillicrap, M. Leach, K. Kavukcuoglu, T. Graepel, and D. Hassabis, “Mastering the game of Go with deep neural networks and tree search,” Nature 529 (7587), 484–489 (2016).

[27] Y. Liu, W. Sun, H. Xie, N. Zhang, K. Xu, Y. Yao, S. Xiao, Q. Song. “Very sharp adiabatic bends based on an inverse design,” Opt. Lett. 43, 2482-2485 (2018).

[28] L. Wang, Y. Luo, Z. Liu, X. Feng, and B. Feng, “Fabrication of microlens array with controllable high NA and tailored optical characteristics using confined ink-jetting,” Appl. Surf. Sci. 442, 417–422 (2018).

[29] S. Surdo, R. Carzino, A. Diaspro, and M. Duocastella, “Single-Shot Laser Additive Manufacturing of High Fill-Factor Microlens Arrays,” Adv. Opt. Mater. 6(5), 1701190 (2018).

[30] J. M. Lourtioz, H. Benisty, V. Berger, J. M. Gerard, D. Maystre, and A. Tchelnokov, Photonic Crystals: Towards Nanoscale Photonic Devices (Springer, 2008).

Chapter 5 TE to TM polarization waveguide rotator based on nano-pixel structure

5.1 Introductory overview

In the development of photonic integrated circuits (PICs), polarization management is an important research topic because of the polarization-dependency of the optical waveguide devices [1]. Polarization rotators, therefore, are often used to manipulate the polarization state of optical wave. As mentioned in Chapter 1.6, traditional rotators are either with a large size, a complex fabrication or a high excess loss [2-11]. In this work, a polarization rotator designed with deep learning has been proposed and demonstrated. The total footprint of the rotator is $2.1 \times 12.58\ \mu m^2$ with the polarization extinction ratio of 25.8 dB and the excess loss of 0.17 dB. Furthermore, the proposed rotator exhibits sufficient fabrication tolerance of ±10 nm (±6.7%).

5.2 Polarization rotator design

The deep learning design process is similar to that of the

optical power couplers mentioned above. Polarization extinction ratio (PER) and excess loss (α) are introduced to evaluate the device performance. PER is defined as the ratio of output optical power of TM polarization to that of the TE polarization. α is the total loss between input waveguide and output waveguides. Our targets are PER > 25 dB and α <0.2 dB.

Figure 5.1(a) shows the finally optimized structure of the polarization rotator couplers, which occupies a 2.10×12.58 μm^2. There are totally 576 circular air holes randomly located in this area to induce a polarization rotating function. These holes are with an identical diameter of 148 nm. In order to achieve single-mode operation around the wavelength of 1620 nm and a low coupling loss between the input / output waveguides and the polarization rotating section, the optimum width is 1 μm for both the input and output waveguides. Here, the reason of choosing the wavelength from 1570-1680 nm is considering the future application of the rotator in the breath sensing chip [13]. The rotator is constructed on a 100 nm Si high-mesa waveguide as shown in Fig. 5.1(b) [13]. In our previous work [13], we have demonstrated that the fabrication of the waveguide was able to be completed in single step etching process and the propagation loss of the waveguide was as low as 0.2 dB/cm.

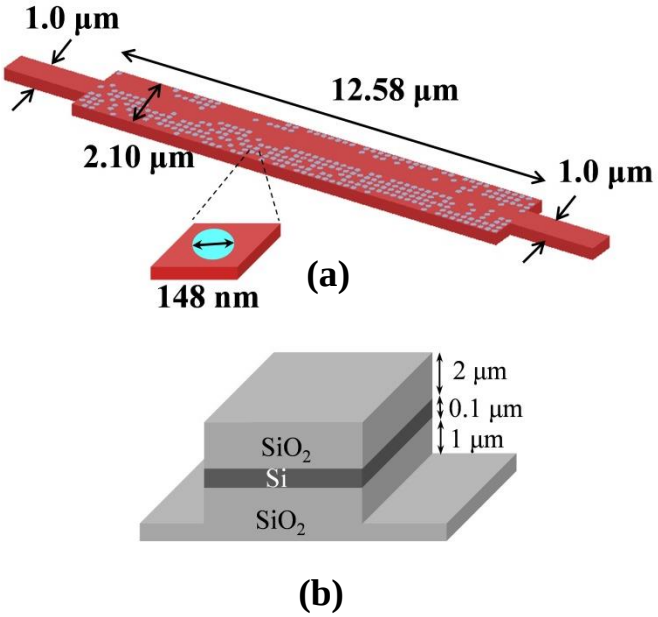

Fig. 5.1 Designed polarization rotator: (a) Schematic diagram: input TE mode is rotated into TM mode by the rotator and (b) 100 nm Si high-mesa waveguide cross-section.

The light propagation in the finally optimized polarization rotator was simulated by using finite difference time domain (FDTD) method at the wavelength of 1620 nm. Note that presently we aim to exploit this device to the wavelength range from 1570 nm to 1680 nm for the purpose of near infrared breath sensing, and this wavelength corresponds to the center wavelength of the purpose [18]. In the simulation, the input light is set as TE polarization, so that only the fundamental TE mode is excited in the input waveguide. Figures 5.2 shows the simulated optical filed of TE and TM polarization in the rotator.

The color bar at the right side of the simulated results indicates the normalized light intensity profile, where different color stands for different light intensity, for example the dark blue means no light.

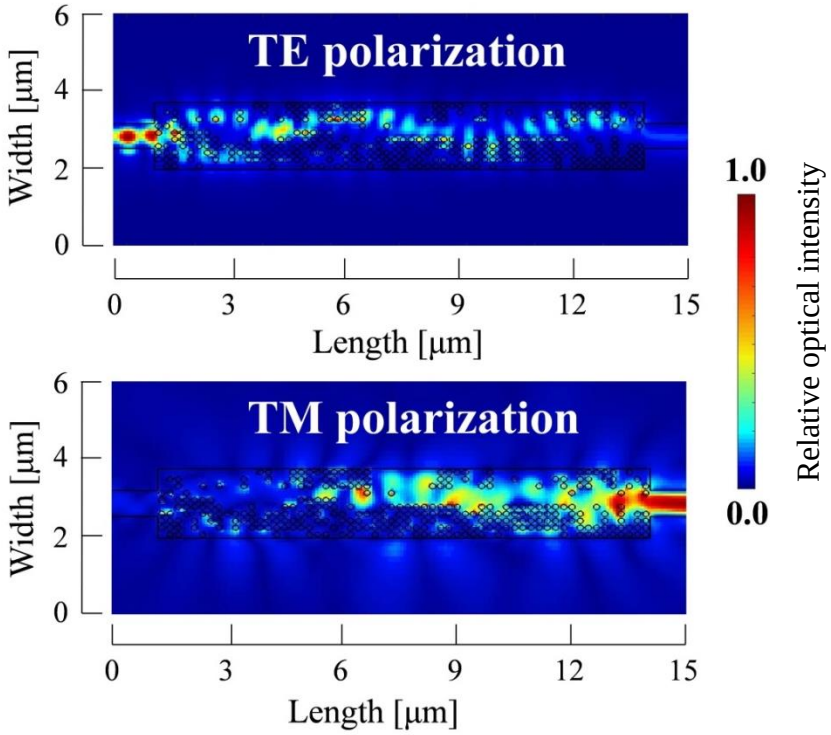

Fig. 5.2 Designed result: simulated light propagation in the polarization rotator of TE polarization (top) and TM polarization (bottom). The left bar is the relative optical intensity in the waveguide: 1.0 indicates strongest intensity and 0.0 is no light.

We can see that the TE polarization light is weakened gradually along the rotation section and almost disappears at the output port. In contrast, TM polarization is strengthened gradually along the rotation section and the TE polarization is almost totally rotated into TM polarization at the output port.

According to our calculation, PER is 25.8dB, which verifies the polarization rotating function of the inversed designed structure in Fig. 5.1. The calculated α is as low as 0.17 dB, which is important for realize a low loss integrated photonic chip.

5.3. Wavelength dependent performance and fabrication tolerance

An important characteristic for the polarization rotator is the wavelength dependent performance shift. Figure 5.3(a) shows the PER from 1570-1680 nm, which indicates that the device has a low wavelength dependent performance shift in this range. This ability proves a broadband application in future integrated photonic circuits. Figure 5.3(b) exhibits the relationship of the excess loss α and working wavelength. α is keeping lower than 0. 4 dB from 1570-1680 nm, which is important for realize a low loss integrated photonic circuit.

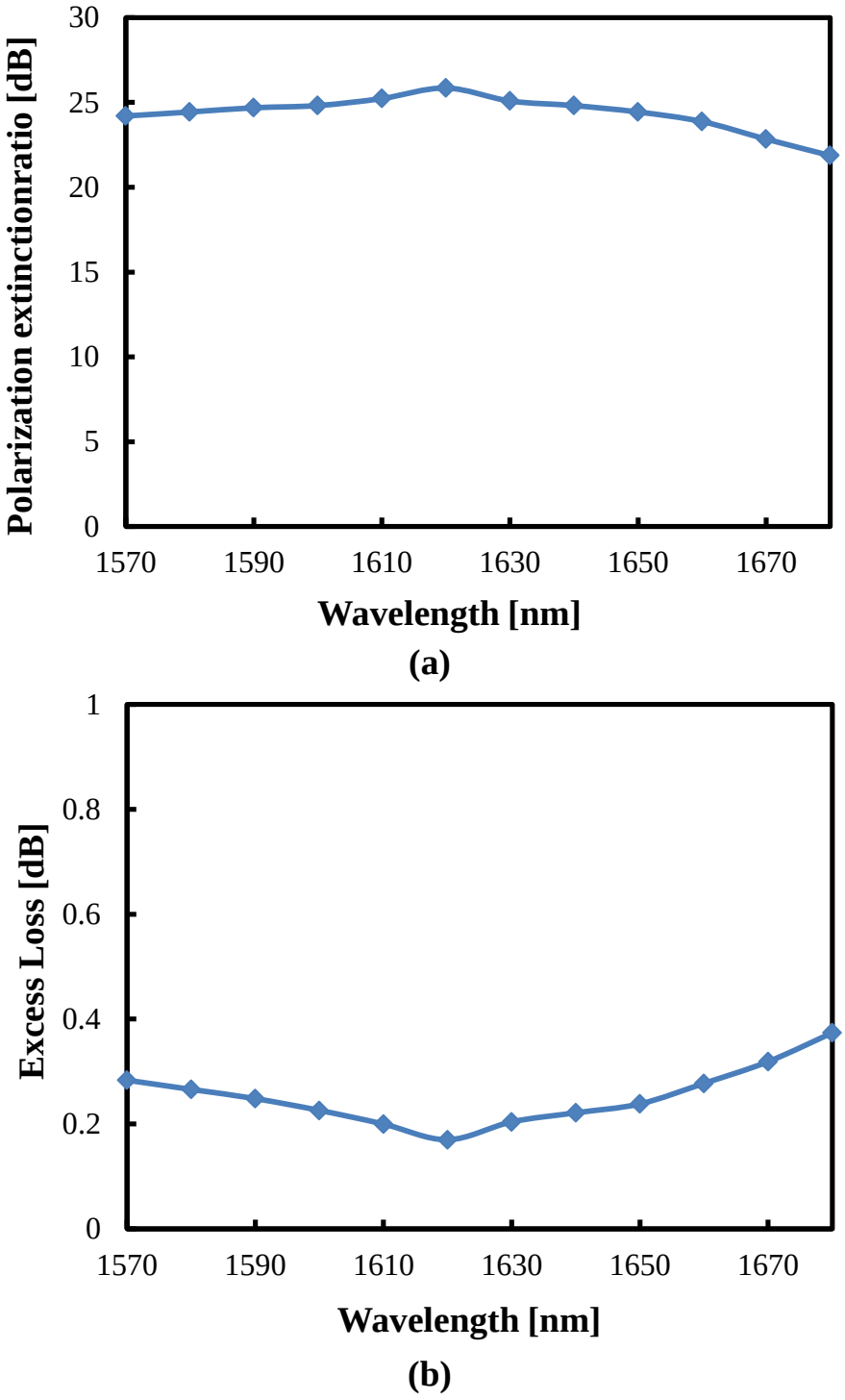

Fig. 5.3 Calculated wavelength dependent performance (a) polarization extinction ratio and (b) excess loss.

For the future application of the polarization rotator, a high technological fabrication tolerance has to be fulfilled. The most

critical technological parameter with the largest contribution to the polarization rotation performance is the sizes of the holes. The influence of the hole diameters on the PER of the rotator; therefore; has been calculated. For our device, it is able to be fabricated by using electron-beam lithography with a resolution as high as sub-10 nm. Considering this resolution, the diameter has been varied over a certain range from 138-158 nm in the calculation, while keeping the other parameters constant. Figure 5.4 shows the calculated PER with different diameters. We can see that the change of the PER is sufficiently low in the range of 138-158 nm. PER is 25.45 dB at the diameter of 138 nm and 25.42 dB at 158 nm. The insensitivity of the polarization rotation performance to the diameters of the holes predicts excellent robustness of the device against fabrication imperfection.

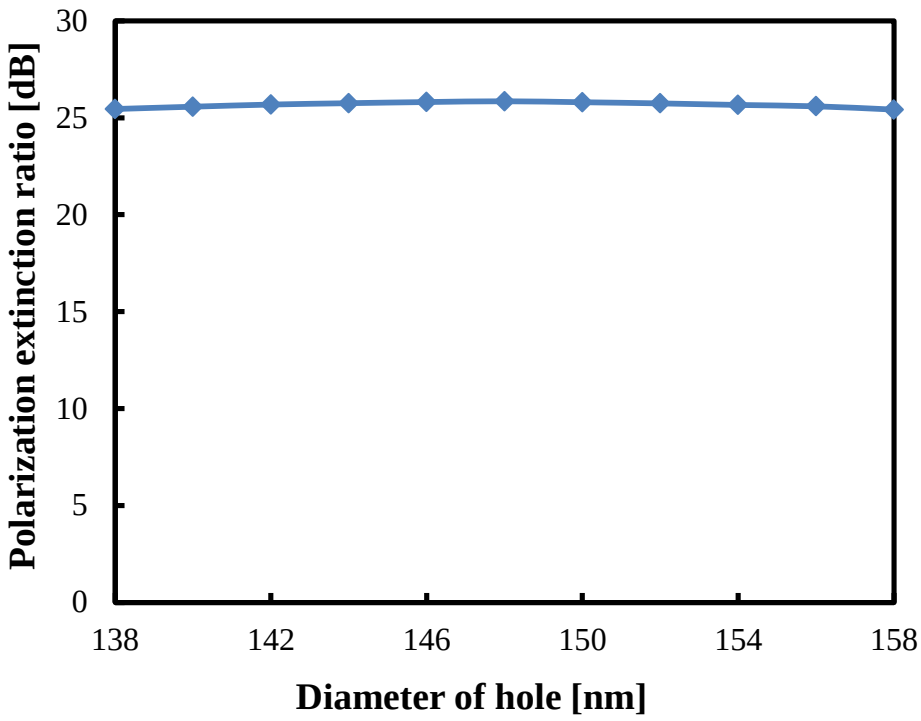

Fig. 5.4 Polarization extinction ratio versus diameter of hole

5.4. Conclusions

We have proposed a compact polarization rotator based on deep learning. The polarization rotation section occupies a footprint of 2.10 × 12.58 μm^2. The estimated polarization extinction ratio was 25.8 dB at the wavelength of 1620 nm. The fabrication tolerance and wavelength dependent performance shit is also examined, and the results show that the device has a tolerance of ±10 nm (±6.7%) and an application window from 1570-1680 nm.

5.5 References

[1] W. Bogaerts, R. Baets, P. Dumon, V. Wiaux, S. Beckx, D. Taillaert, B. Luyssaert, J. V. Campenhout, P. Bienstman, and D. V. Thourhout, "Nanophotonic waveguides in silicon-on-insulator fabricated with CMOS technology," J. Lightwave Technol. 23, 401 – 412 (2005).

[2] T. Barwicz, M. R. Watts, M. A. Popović, P. T. Rakich, L. Socci, F. X. Kärtner, E. P. Ippen, and H. I. Smith, "Polarization-transparent microphotonic devices in the strong confinement limit," Nat. Photonics 1, 57 (2007).

[3] H. Fukuda, K. Yamada, T. Tsuchizawa, T. Watanabe, H. Shinojima, and S. Itabashi, "Silicon photonic circuit with polarization diversity," Opt. Express 16(7), 4872–4880 (2008).

[4] N. Somasiri, B. M. A. Rahman, and S. S. A. Obayya, "Fabrication tolerance study of a compact passive polarization Rotator," J. Lightwave Technol. 20 (4), 751–757 (2002).

[5] H. Deng, D. O. Yevick, C. Brooks, and P. E. Jessop, "Design rules for slanted-angle polarization rotators," J. Lightwave Technol. 23 (1), 432–445 (2005).

[6] C. Brooks, P. E. Jessop, H. Deng, D. O. Yevick, and G. Tarr, "Passive silicon-on-insulator polarization-rotating waveguides," Opt. Eng. 45 (4), 044603 (2006).

[7] H. Deng, D. O. Yevick, C. Brooks, and P. E. Jessop, "Fabrication

tolerance of asymmetric silicon-on-insulator polarization rotators," J. Opt. Soc. Am. A. 23 (7), 1741–1745 (2006).

[8] L. M. Augustin, J. J. G. M. van der Tol, E. J. Geluk, and M. K. Smit, "Short Polarization Converter Optimized for Active–Passive Integration in InGaAsP–InP," IEEE Photon. Technol. Lett. 19 (20), 1673–1675 (2007).

[9] Komatsu, K. Saitoh, and M. Koshiba, "Compact polarization rotator based on surface plasmon polariton with low insertion loss" IEEE Photonics J. 4, 707–714 (2012).

[10] L. Gao, Y. Huo, J. S. Harris, and Z. Zhou, "Ultra-compact and low-loss polarization rotator based on asymmetric hybrid plasmonic waveguide," IEEE Photonics Technol. Lett. 25 (21), 2081–2084 (2013).

[11] J. N. Caspers, J. S. Aitchison, and M. Mojahedi, " Experimental dem-onstration of an integrated hybrid plasmonic polarization rotator," Opt. Lett., 38 , 4054 – 4057 (2013).

[12] A. Michaels and E. Yablonovitch, "Inverse design of near unity efficiency perfectly vertical grating couplers," Opt. Express 26, 4766–4779 (2018).

[13] A. Y. Piggott, J. Petykiewicz, L. Su, and J. Vučković, "Fabrication-constrained nanophotonic inverse design," Sci. Rep. 7, 1786 (2017).

[14] A. Michaels and E. Yablonovitch, “Leveraging continuous material averaging for inverse electromagnetic design,” Opt. Express 26, 31717–31737 (2018).

[15] B. K. Jennison, J. P. Allebach, and D. W. Sweeney, “Efficient design of direct-binary-search computer-generated holograms,” J. Opt. Soc. Am. A 8, 652–660 (1991).

[16] Y. Han, Z. Chen, L. Wang, W. Li, H. Jiang, and K. Hamamoto, “Asymmetric-ration Optical Power Couplers Based on Nano-Pixel Structure,” OSA Continuum, Submitted (2020).

[17] Y. Han, W. Li, Z. Hui Chen, H. Jiang, and K. Hamamoto, “Fabrication and analysis of low loss silicon high-mesa waveguides,” Appl. Opt. 59 (16), 4964-4969 (2020).

[18] W. Li, Y. Han, Z. Chen, H. Jiang, and K. Hamamoto, “Amplifier-assisted CRDS (cavity ring-down spectroscopy) toward compact breath sensing,” Jpn. J. Appl. Phys. 58, SJJD01 (2019).

Chapter 6 Conclusion and outlook

6.1 Conclusion

As mentioned in Chapter 1, rapid aging is becoming one of the most serious issues around the world. As the consequence, health-monitoring has been paid with much attention in recent years. Breath sensor is highly desired for daily health-check due to its noninvasive and convenient fashion for health-monitoring. Breath sensing based on infrared optical absorption could achieve rapid response-time and different gas identification [12]. In order to detect ppm-order breath content in addition to the real time sensing, breath sensing system based on cavity ring-down spectroscopy (CRDS) technique has been researched as a candidate. Compared to the conventional large size CRDS system, a future version of CRDS photonic integrated circuit has been proposed. This brings the possibility of integrating the whole sensing system into a cell phone for real-time health-monitoring. On the circuit, the optical devices, including the sensing waveguides, optical power couplers and polarization rotators, are critical for realizing compact and highly sensitive CRDS.

In Chapter 2, the principle of gas sensing by using waveguide has been discussed and deep learning assisted optical design has been introduced. Based on these two gas sensing principles, we discussed the possibility of using waveguide sensing CRDS photonic chip to detect breath content. The results show that the ppm-order breath sensing is possible by using the waveguide CRDS photonic chip. In order to design the optical power couplers and polarization rotator, we compared the traditional optical design method and deep learning method. The traditional design method has led to many useful devices in the past, its limitation becomes apparent when designing more a complicated device. In contrast, deep learning has the ability to solve the problem.

In Chapter 3, thin silicon (Si) waveguides with a Γ_{air} as high as 37.6 % have been proposed and fabricated. Thermal oxidation technique was applied to further reduce α, so that α was decreased from 1.45 to 0.84 and 0.29 to 0.2 dB/cm for the 0.5 and 3μm-wide waveguide, respectively. According to our analysis, the significantly decreased α is attributed to recovering the damaged Si core and smoothing the waveguide sidewalls. The high Γ_{air} and effective loss reduction show a promising potential of applying Si high-mesa waveguides to realize

ppm-order sensing.

In Chapter 4, we have designed optical power couplers with a splitting power ratio 1:9 and 1:99. The different ratios are realized via deep learning optimizing nano-pixels. The coupler performance of every trial is evaluated by FDTD method. The optimization of the output waveguide positions and widths was applied to reduce α. After the optimization, α was effectively reduced from 3.7 to 0.3 and 3.62 to 0.27 dB for the1:9 and 1:99 coupler, respectively. In order to enhance the applicability, the output and input waveguides should have the same width, so a mode size converter is designed also via deep learning design at the input side to widen the 0.5 μm -wide waveguide to 1 μm. The converter demonstrates a loss of 0.045dB, a footprint of 1×2 μm^2. The whole devices have an operation wavelength from 1500 to 1600 nm with a fabrication tolerance of ± 10 nm (± 11%).

In Chapter 5, we have proposed a compact polarization rotator based on deep learning design. The polarization rotation section occupies a footprint of 2.10 × 12.58 μm^2. The estimated polarization extinction ratio was 25.8 dB at the wavelength of 1620 nm. The fabrication tolerance and

wavelength dependent performance shit is also examined, and the results show that the device has a tolerance of ±10 nm (±6.7%) and an application window from 1570-1680 nm. The results reveal the promising potential of the deep learning designed rotator to be applied in integrated photonic circuits.

The demonstrated optical devices will pave the way for developing compact CRDS photonic integrated circuit.

6.2 Outlook

We have demonstrated the sensing waveguides, optical power couplers and polarization rotators for realizing future CRDS photonic integrated circuit. To complete the whole CRDS circuit; however; some issues are needed to be discussed.

First is the light source. In order to sensing several gases, a multi-wavelength light source is expected. One candidate is the SLED (super luminescent diode), which emits light at a wide range of wavelength. If the SLED is selected as the laser source, a wavelength division multiplexer is needed at the sensing system output part in order to separate the light at gas absorption wavelength. Wavelength tunable laser is also a candidate, as its wavelength of operation is able to be altered in a controlled manner. By choosing the target gas, the wavelength tunable laser

emits the light at the absorption wavelength of the gas we choose.

Second is the amplifier. One candidate of on-chip amplifier is semiconductor optical amplifiers (SOA). Based on our knowledge, SOA normally works in C-band (wavelength from 1530 to 1565 nm). The light at wavelength larger than 1600 nm is hardly to be amplified by SOA. The amplification for 1650 nm (methane absorption wavelength) and 1680 nm (acetone absorption wavelength) need to be carefully considered.

Finally, we believe that the demonstrated optical devices will contribute to realize hand-held size breath sensor in future.

Appendix

A-1 Symbols used in this thesis

Symbol	Meaning
α	Propagation loss
Γ_{air}	Portion of light profiles that comes out of waveguide
N’	Density of the gas molecule
σ	Gas absorption cross-section
L	Interaction length between sensing light and the garget gas
I_{in}	Input light intensity
I_{out}	Output light intensity
NA	Avogadro constant
n	Amount of the target gas
V_{total}	Total volume of the breath
V_{gas}	Volume of the target gas
P	Pressure

T	Temperature
R	Ideal gas constant
τ_0	Decay life of the light in gas-cell
τ	Cavity ring-down time in the “no-gas in gas-cell” situation
T_{gas}	Cavity ring-down time in the “gas in gas-cell” situation
t	Time
c	Light speed
k	Boltzmann constant
L	Waveguide length

A-2 Finite difference time domain method (FDTD)

The finite difference time domain (FDTD) method is an exact solution to Maxwell’s equations. It does not have any theoretical restrictions or approximations. FDTD is widely utilized as a propagation solution method in integrated optics, especially when the adequate solutions are not obtainable by other methods, such as BPM (Beam Propagation Method). As shown in Fig. A1,

an optical structure based on nano-pixels is simulated by utilizing FDTD. FDTD can cancel the round-off errors which could happen in BPM. FDTD could do this calculation in tow or in three dimensional processes.

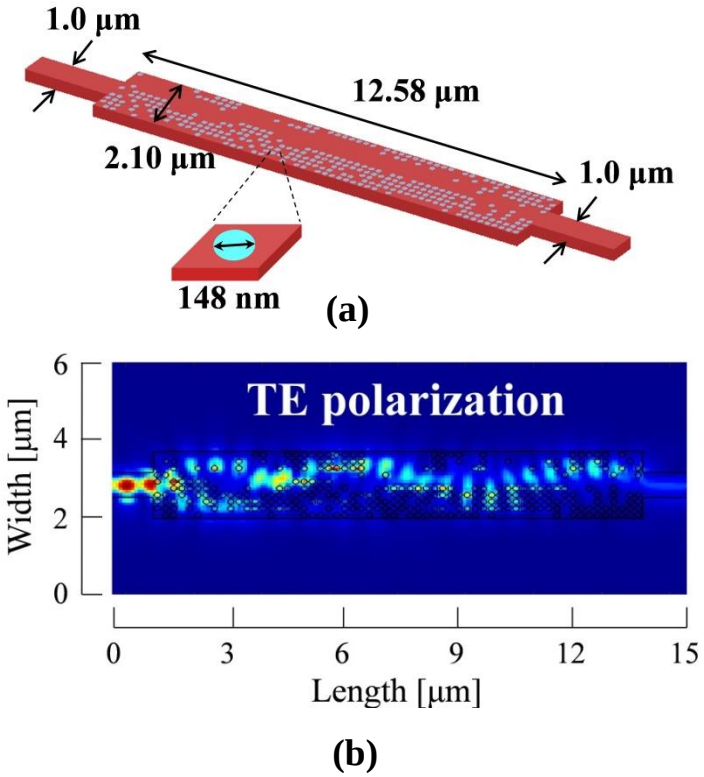

Fig. A1 An example of FDTD simulation (a) Optical structure and (b) simulated TE polarization light propagation in the structure.

Acknowledgement

I would like to thank everyone who helped me with this project. In particular, I would like to thank my supervisor Prof. Kiichi Hamamoto for his giving me such a chance to study here, his attention and care all the time and his technical support and guidance.

I would also like to thank Prof. S. Yokoyama and Prof. D. Wang for their assistance with optical devices fabrication and discussion. Thanks to all members of Hamamoto’s Lab for their help in my ordinary life. At last, I would like to thank my family.